REVIEW ARTICLE

Synchrotron Radiation in Biology and Medicine

J.B. Pełka*

Institute of Physics, Polish Academy of Sciences, Al. Lotników 32/46, 02-668 Warsaw, Poland

Received: 08.11.2021 & Accepted: 21.12.2021

Doi: 10.12693/APhysPolA.141.3 *e-mail: pelkay@ifpan.edu.pl

The properties of synchrotron radiation, substantial for biomedical research, as well as basic methods using these sources are briefly discussed. Particular attention is paid to radiation damage, which imposes the modification of techniques and procedures for synchrotron research in biology relative to the approach in materials science. The principles and the stormy development of new basic techniques such as imaging, structural and ultrafast dynamics studies developed for free-electron lasers are briefly reported. A special section is dedicated to the latest research with terahertz radiation on detection of pathogens, including viruses, as a possible application of synchrotron technology. Recently achieved viral detection sensitivity and selectivity are comparable to classical bioanalytical methods. This review is intended to researchers of various science and technology disciplines with, who are interested to cooperate in application of synchrotron radiation for issues of biology and medicine and provides a set of relevant references.

topics: synchrotron radiation, free-electron laser, biomedical applications ,radiation damage

1. Introduction

The methods using synchrotron radiation (SR) in biological and medical applications have been intensively developed for over 50 years. Since the beginning of the 21st century, research in this field has accounted for a rapidly growing share of the total beam time allocated at most of medium and large synchrotron sources — the accumulation rings and Free Electron Lasers (FEL). Today they take far more than half of the accessible beam time. This fact alone, taking into account the significant increase in the number and efficiency of the available synchrotron beam lines, indicates the importance of synchrotron sources for the stormy development of research related to life sciences.

Almost any of the synchrotron research techniques applied to non-biological condensed matter can be used, with some modifications, to study biological objects. The principles of measurement, the physical foundations and the methods of interpretation are essentially similar for "non-biological" and "biological" cases. However, living organisms and their constituent parts are, by their nature, notably different from other types of matter. Their specific properties require special care during the experiment and the preparation of the research material. This imposes strict requirements on the quantities of admissible doses and extorts the use of precise radiological protection procedures for both the tested biological systems and the experimenters due to the ease, the intense beams of synchrotron radiation can modify and destroy objects with which they interact.

It can already be seen from the above that the thematic scope of this work is extremely wide and, by necessity, had to be significantly limited. It does not contain many interesting issues from nearby disciplines, such as regenerative medicine with tissue engineering and the search for materials to replace damaged bone fragments, joints and soft tissues [1]. There was also no room for such seemingly distant fields as archaeometry supporting the study of cultural heritage with the methods of natural sciences, drawing more and more boldly from synchrotron applications in the field of bioorganic artifact analysis [2, 3]. Recently, ancient papyrus scrolls, made of natural organic matter, stuck together, or even burned, have been successfully read without the need for destructive unfolding, using phase contrast SR microtomography [4–6]. Many examples of biomedical applications of synchrotron radiation can be found in the publications included in the references.

As a natural consequence of the interdisciplinarity of this field of research, it is obvious that research success can be achieved only by combining the cooperation and experience of physicists, biologists, medical doctors, engineers and IT specialists. Collaboration presupposes mutual understanding. Helping this is one of the important goals of this work.

The detailed knowledge of the elemental composition and distribution in an object exposed to ionizing electromagnetic radiation is crucial to determine the dose that will be absorbed as a result of irradiation. This, in turn, makes it possible to assess the possible typical radiation damage in biological structures. Living organisms mainly consist of light elements [7–10]. For example, it was determined that the content of some trace elements — transition metals and zinc in phytoplankton and bacteria often meets a simple stoichiometric formula $Fe_1Mn_{0.3}Zn_{0.26}Cu_{0.03}Co_{0.03}Mo_{0.03}$ [11]. The average density of most of these microscopic organisms is close to that of water. Cell density depends somewhat on the phase of the life cycle. The largest is in the phase between DNA replication and nuclear division [12, 13]. The average mammalian DNA density was determined as 1.705 g/cm^3, and for proteins as 1.35–1.43 g/cm^3 [14][†1]. Biological systems are characterized, among others, by the enormous complexity of structures and connections between individual components. Structural order, such as in the case of a silicon crystal, is extremely rare in living organisms, although there are examples of animal organs with a surprisingly high degree of order. An example can be microlenses, hundreds of which are distributed over the entire surface of the brittle star (*Ophiocoma wendtii*), made of calcite crystals in such a way that the optical axis of each lens coincides with the *c*-axis of the calcite crystal, thus eliminating the problem of birefringence [15]. Another example, on a larger scale, is the highly ordered distribution of hexagonal cone-shaped ommatidia in the eyes of the ruddy darter (dragonfly *Sympetrum sanguineum*, see Fig. 1a) [16, 17]. As a rule, however, even where a clear structural order can be seen, it is not perfect. A characteristic example is the quasi-photonic structure of the wings of many birds and insects, responsible for the formation of so called structural colors, e.g. wings of the butterflies of the *Morpho* family — intense blue-green colors dependent on the angle of view, or the layered structure of the iridescent wing covers of some beetles (see Fig. 1b) [18–21]. Structural ordering in biology is implemented to the extent that it supports the function of a given structure, cell, tissue or organ.

The tissues are composed of many types of materials. "Soft" materials include fibers, membranes, gels, and tissues composed of organic molecules of various sizes and types. Inorganic particles such as silicates, carbonates, phosphates and oxides are the building blocks of a scaffold (e.g. bone) that strengthen and stabilize "soft" tissue structures. They also exist as materials for special purposes, for example in the form of magnetic microstructures constituting the basis of one of the two types of

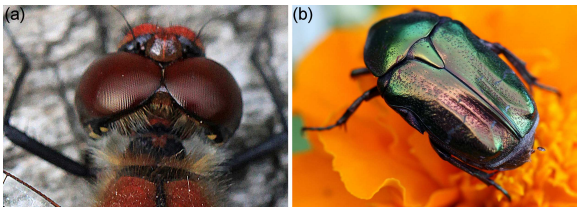

Fig. 1. (a) Compound eyes of a male ruddy darter (dragonfly *Sympetrum sanguineum*) with highly ordered array of hexagonal cone-shaped ommatidia. (b) The European rose chafer (*Cetonia aurata*). The shimmering colors of its wing covers are the result of light scattering on a complex multilayer structure in which the individual layers are quite irregular while maintaining an average thickness. Additionally, it was found that the wing covers of this beetle reflect only left-circularly polarized light (Author's photos).

senses for the magnetic orientation of animals in the Earth's magnetic field [22–25][†2] Some of these materials perform their functions directly in the form of nanostructures. Examples include the coding and storage of genetic information by DNA or the mobility of cells achieved through the polymerization and depolymerization of actin. Sub-micron-sized elements combine into larger units that perform the same function as muscles and tendons or the walls of plant cells. In all these examples, the nanoscale plays an essential role. Structures commonly found in living organisms can be imagined as composed of elementary bricks with dimensions of the order of nanometers: proteins, nanofibers, membranes or mineral particles, containing a multitude of interfaces and interphases. These bio-nanostructures perform many basic functions in living organisms, from energy conversion to chemical synthesis and mechanical stabilization, merging into larger functional structures such as cells, tissues and organs. With this complexity, there is a need to properly identify the structures and processes relating to the function or property of the object that we intend to study. This task is incomparably more difficult in relation to the degree of complication found in objects built of inorganic matter.

Synchrotron radiation brings many new research opportunities. The relationship between structure and function can be determined in some cases by *in situ* and *in vivo*, by studying dynamics of undergoing processes with picosecond, and more recently with femtosecond resolution, the dynamics of biochemical reactions, phase transitions, or response

[†1]Discrepancies due to the method of determination.

[†2]More recent studies indicate the prevalence of the second type of magnetic sense, based on processes taking place in pairs of radicals formed by cryptochromes. They are also to be found in the plant kingdom. There are also reports entirely challenging the traditional view on the role of magnetic microcrystals placed in the middle ear of birds [25].

to an external stimulus, such as a change in temperature, magnetic field, toxin attack or mechanical stress. The study of the relationships between the function, structure and dynamics of biological processes at various levels of their organization is one of the most important applications of SR.

The diversity and dynamics of life processes are characterized by exceptional richness. Typical time scales of these processes range from tens of femtoseconds for fast photosynthetic reactions, through picoseconds needed for example for oxygen atom binding to the heme component of Hb, to nanoseconds or hundreds of seconds where some interactions that control life processes, most enzymatic processes, and creation as well decay of biological structures responsible for life take place. Relatively slow processes such as endocytosis, apoptosis, and mitosis usually consist of sequences of faster subprocesses, such as enzymatic reactions, molecular diffusion, and the formation/breaking of protein–ligand bonds. This means that the precise study of many biological processes requires the use of techniques that capture their course in very short periods of time. Synchrotrons, as pulsed radiation sources, are an excellent tool for studying the dynamics of processes in various photon energy ranges with a temporal resolution of up to several dozen picoseconds[†3]. The most advanced and strongest sources of ionizing electromagnetic radiation, which are short-wave Free Electron Lasers FEL, move even lower on this scale. They emit ultra-short pulses of monochromatic photons with a duration of the order of several to several dozen fs and with a peak power reaching even a dozen or so GeV.

The dynamics of the processes are usually studied using one of the Pump and Probe (P&P) methods. They consist in triggering the examined process (with a "pumping impulse") and monitoring a physical state characterizing the process at a given interval, or a series of intervals determined by means of a closely synchronized "probe pulses". In general both pump and probe pulses do not have to be electromagnetic in nature, but in this work we only deal with ultrashort pulses of light. The use of high-brightness synchrotron sources has significantly deepened our understanding of many phenomena and processes including at the interface between the organism and inanimate matter (aquatic environment/microorganism, mineral/microorganism, soil/plant etc.). More about the P&P methods can be found in Sect. 4.3.

Synchrotron radiation makes a significant contribution by exploring the synthesis, adaptation, and repair strategies nature uses to build, operate, and "heal" these usually very complex systems. Research with its help also often has direct medical implications. The great challenge is to create artificial systems that recreate the functions of cells or even entire organs (artificial life), biosensors implanted *in vivo*, or drug carriers. Synchrotron research in the field of biology also contributes to the development of materials engineering. Along with large-scale efforts to develop new directions of regenerative medicine, it becomes necessary to develop reliable materials that could be safely hybridized with living systems. They also make a significant contribution to the development of material biomimetics, based entirely on knowledge of the structure and operation of natural systems.

Proteins are the basic component of dry cell mass (depending on the type from 40% to 70%) [26]. Over the past decade, the world of proteins with known amino acid sequences has expanded rapidly. Currently, the UniProtKB/TrEMBL databases contain data on the sequences of millions of proteins or their characteristic fragments, of which over 500 000, described and pre-verified, are included in a separate Swiss-Prot database [27]. So far, the spatial structures of over 183 000 of these proteins have been determined and collected in the PDB database[†4]. Today, the basic tool for studying the structure of proteins is synchrotron radiation. Almost 90% of these structures were determined using the MX diffraction lines of synchrotrons, mainly of the 3rd generation. This great disproportion between the number of proteins with a known sequence and those with a known structure illustrates the amount of work to be done.

Unfortunately, it is estimated that about 40% of proteins cannot be crystallized by any known method or only small, difficult to purify nanocrystals are obtained, not suitable for determining the structure by conventional crystallographic methods. Among them are majority of Membrane Proteins (MP) which are crucial in "servicing" the border between the cell and the outside world, including the transport of drugs into cells. Significant progress in the study of the structure of these difficult-to-crystallize biomolecules has come only recently with the advent of the X-ray Free Electron Lasers (X-FEL). The first 64 protein structures determined using these most advanced X-ray sources were included in the PDB database at the end of 2016. At the beginning of 2021, there were already several hundred of them.

In the last decade, the genomes of many organisms have been sequenced. On this basis, it is known that as much as 30–40% of all encoded proteins are metalloproteins [28–30]. Metal ions are essential to many fundamental biological processes in organisms. Metalloproteins are critical to a number of

[†3]We do not mean here a rarely used technique called "femtoslicing", which allows to receive femtosecond radiation pulses of very low intensity (in the order of 100–1000 photons/sec) from undulator at an ordinary synchrotron

[†4]As at the end of September 2021.

metabolic processes, such as energy conversion in photosynthesis and respiration, and the molecular signaling processes that govern gene expression and regulation. New, post-genomic areas of science have emerged — metallomics and metalloproteomics, dealing with the analysis of all issues related to the presence and activity of metals in cells and tissues [31–33]. Synchrotron methods for investigating X-ray absorption play a special role in this type of research. They allow to determine not only the distribution of atoms of a given element in a cell or tissue with extraordinary sensitivity and spatial resolution, but also to examine the valence and the chemical environment of the atoms.

Macromolecular (MX) crystallography is currently one of the most important applications of synchrotron radiation in life sciences. Strong monochromatic X-ray beams with photon energies precisely matched to the needs play a fundamental role in modern structural biology. Details of the MX method, as they are beyond the scope of this work, can be found elsewhere, e.g. in the work of M. Jaskólski [34] and the references cited therein.

Synchrotron radiation applications extend far beyond the structure determination of key building blocks of organisms, such as the proteins and other biomolecules. With its help, you can take a deepen look into dynamical phenomena serving biological processes, fundamentals of functioning the multistory structures of life. Controlling metabolic processes, e.g. for medical therapies assumes a thorough understanding of their chemical, electronic, optical and many other properties. The vastness of these tasks requires use of a wide range of highly sensitive methods from imaging to diffraction and numerous spectroscopies of photons and electrons in wide range of excitation energies. New SR-specific diagnostic and therapeutic promising techniques for clinical applications in living patients have been emerged in last three decades, being now in various phases of development [35].

The limited capacity of the article forces to select only the most important issues related to its subject, the most important, common for research applications using SR sources to study the structures and processes of life. The following parts will be focused on recalling the basics of the interaction of strong synchrotron radiation beams with biological matter, systematic characterizing individual spectral ranges of SR in the context of experimental techniques in biology and medicine. Next, we will deal with radiation damage, a phenomenon which fundamentally affects synchrotron methods and procedures biological objects research. We will also briefly describe the latest sources of SR, namely free electron lasers, with the advent of which a new stage in the development of research methods in life sciences and medicine technologies begins. Finally, we will deal with the selected issues of research with the use of SR.

The nature of the experiment in the field of life sciences using synchrotron radiation requires a combination of knowledge and professional experience of representatives of many specialties. On the one hand, biologists and medical doctors, on the other, physicists, technicians and engineers. The condition for efficient cooperation of participants in a specific research project is a mutual understanding of the substantive foundations and the research methods used. This work, presenting selected issues important for the application of synchrotron radiation in biomedical sciences, was intended to support this goal.

2. The interaction of SR with biological objects

The spectral range of radiation produced by present synchrotron sources (bending magnets, wigglers and undulators installed in the storage rings, and free electron lasers) extends from terahertz waves ($\lambda = 1000$ μm, $\nu = 3 \times 10^{11}$ Hz, $E = 1.24 \times 10^{-3}$ eV) up to Hard X-rays (HX), ($\lambda = 2.48 \times 10^{-3}$ nm, $\nu = 1.208 \times 10^{20}$ Hz, $E = 500$ keV) [36]. In the first approximation, the interaction of radiation with condensed matter can be described synthetically by means of the absorption coefficient, or its reciprocal — the absorption length (penetration depth)[†5].

The absorption of a substance at a given wavelength is influenced by the sum of many mechanisms of interaction of electromagnetic radiation with the sample. Different mechanisms of interaction between radiation and matter dominate in individual spectral ranges. The basic factors affecting absorption, in addition to the atomic/molecular composition and material density, may also include internal structural order and the orientation of the sample with respect to the incident beam. Important factor in some ranges can be sample temperature. It happens, e.g. when temperature phase transition in the material occurs. It is the case of water and ice in the terahertz range of radiation. Water as a polar solvent strongly absorbs radiation in this range, but ice as a non-polar substance is almost transparent. Also the high energy density (intensity) of the beam may alter absorption by increased contribution of nonlinear effects. Unless we specifically mention it, in Sect. 2 we will assume that the incident beam is weak enough to neglect these effects.

The basic mechanisms for scattering/absorption, i.e., Rayleigh, photoelectric effect, Compton scattering, pair production and spectral ranges which contribute significantly are not specific to biological

[†5]We mean the linear absorption coefficient, which will be used in most cases in this work, unless the context indicates otherwise.

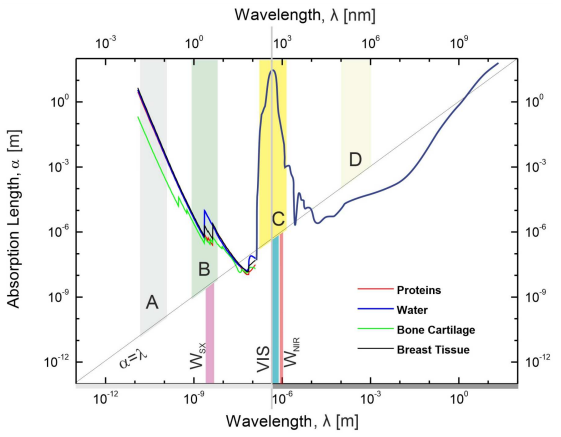

Fig. 2. Wavelength ranges particularly useful in the study of biological objects. The bold grey part of the bottom λ-axis indicates the non-ionizing part of electromagnetic waves. Comments in the text.

problems. Their detailed description can be found in numerous textbooks on the interaction of electromagnetic radiation with condensed matter.

For research in the field of biology and medicine, basically the entire spectrum of radiation produced by synchrotrons can be used — from the longest wavelengths in the terahertz range, through infrared, visible area, ultraviolet, as well as Soft and Hard X-rays. For practical reasons, synchrotron radiation with wavelengths, which are the domain of optical lasers, is less often used — the lasers are smaller and cheaper. Sometimes however, it is convenient to use a synchrotron source also in this wavelength range, e.g. due to the relatively easy tunability of synchrotrons. Pulsed lasers are however often used together with synchrotrons as sources of a second "color" for pumping or, less likely, probing wavelength in variants of P&P methods.

In order to characterize the individual radiation ranges for biomedical applications, it is useful to refer to the dependence of the radiation absorption length (penetration depth) as a function of the wavelength for liquid water, which is a common solvent, essential for living organisms. It is shown in Fig. 2 with the curve marked in blue [37][†6]. It is also typical of many biological materials, with the exception of extreme transparency in the visible range and very strong absorption in the terahertz range observed for liquid water [38–40]. In Fig. 2, for comparison, also a typical profile of absorption length α for the proteins and two tissues: breast tissue and cartilage are shown. Straight line along the diagonal stands for loci with $\alpha = \lambda$, that is where the absorption length is equal to the wavelength[†7]. Below, three wavelength subranges are marked: Soft X-ray Water Window (WSX), Visible Spectrum (VIS) range, and Near Infrared Water Window Range (WNIR). They will be discussed later on. It can be assumed that the ranges useful for imaging in the transmission modes are those in which the penetration depth is significantly greater than the wavelength.

Figure 2 distinguishes two such areas suitable for imaging biological samples, B — in the Soft X-ray range, and C — covering the wavelength range around the Visible Spectrum (VIS) from the Ultraviolet (UV) to the Near Infrared (NIR). An excessively large absorption length makes the samples too transparent. This may reduce the vertical resolution of the imaging due to overlapping images of different depths, even at a relatively shallow depth of field. The optimal wavelength ranges are those for which the penetration depth is somewhere between 10^2 and 10^4 wavelength (the values given here are only indicative, much depends also on the depth structure of the sample and its total thickness). From this point of view, the region B in the SX range from 1 to 5 nm turns out to be roughly optimal for X-ray absorption microscopy. The absorption length in this area for biological samples corresponds to sample thicknesses of a few μm.

For X-ray crystallography, which requires larger sample volumes/thicknesses to obtain adequate resolution, to take full advantage of the periodicity of unit cells ordering, optimal penetration depths are greater, in the order of 10^8–10^{10} wavelength — the appropriate area is marked as A. The D area is located in the terahertz range. For water, which is a polar liquid, it does not meet the stated criterion for a "good" imaging range. However, for ice and other anhydrous materials, including non-polar solvents, this range is quite useful for both imaging methods and spectroscopy.

2.1. Applications of particular ranges of synchrotron radiation

We will start our overview of the radiation ranges from the short-wavelength, ionizing part of the spectrum. A significant part of the applications of synchrotron radiation in biology and medicine requires beams of particularly high intensity and wavelengths in the Hard X-ray (HX) range, along with the Soft X-ray (SX) range. This applies especially to the imaging diagnostics of thicker tissue layers. These requirements are best met by synchrotrons with an electron beam energy of at least 2 GeV and the highest possible current. Additionally, wigglers

[†6]The idea of such a presentation comes from the cited paper by Sayre and Chapman [37], where with this idea the optimal wavelength ranges for microscopic methods were indicated.

[†7]The transmission mode occurs, when the imaged sample is located between the light source and the detector. When the detector location is at the same side as the source, we are dealing with a reflection mode.

TABLE I

Radiological properties of selected tissues for the photons of energy 40, 100 and 300 keV [41].

Material/tissue	Z/A	Mass density ρ [g/cm^3]	Mass absorption coefficient μ/ρ [cm^2/g]			Absorption length α [cm]		
			@ 40 keV	@100 keV	@300 keV	@ 40 keV	@100 keV	@300 keV
fat	0.5558	0.950	0.2396	0.1688	0.1187	4.3933	6.23597	8.8680
water	0.5551	1.000	0.2683	0.1707	0.1186	3.7272	5.85823	8.4317
breast	0.5520	1.020	0.2530	0.1688	0.1179	3.8751	5.80801	8.3155
brain	0.5524	1.040	0.2702	0.1701	0.1181	3.5586	5.65278	8.1417
lung	0.5505	1.050	0.2699	0.1695	0.1177	3.5286	5.61877	8.0916
skeletal muscle	0.5500	1.050	0.2685	0.1693	0.1176	3.5470	5.6254	8.0985
blood	0.5500	1.060	0.2715	0.1695	0.1176	3.4748	5.56576	8.0221
cortical bone	0.5148	1.920	0.6655	0.1855	0.1113	0.7826	2.80773	4.6795

TABLE II

Typical photon energies applied in selected X-ray techniques.

Application	Photon energy [keV]
mammography	17–24
stomatology	60–70
chest radiography	50–70
coronarography	50 (with Gd contrast)
radiotherapy	30–10000
radiotherapy MRT	27–600

or tunable undulators with a strong magnetic field are used as sources to increase the radiation intensity. Maximizing the intensity of the photon beam allows to achieve dose rates in excess of 30 000 Gy/s.

The SR X-ray photon energy applied in medical diagnostics is usually in the range of 10–300 keV. The human body is basically opaque to photons with energies lower than 10 keV, but the spectral range below this energy is used in some diagnostic methods on thin tissue preparations and cells. In clinical X-ray therapy, photon beams with energy up to 30 MeV produced by small electron accelerators, but not obtainable with synchrotrons, are also commonly used. Values of absorption at selected photon energies are presented in Table I, and typical photon energies applied in various technique of X-ray imaging and radiotherapy in Table II.

2.1.1. Hard X-ray range (HX), 0.25–0.00248 nm, 5–500 keV

The lower limit of the energy range of Hard X-ray photons is not unequivocally established and depends on the adopted criterion. Here, the lowest limit is given due to the limitations of absorption by the beryllium window and the possibility of measuring in air.

The basic processes of X-ray beam interaction with matter in the HX range are the photoelectric effect, Compton scattering and Rayleigh scattering. The first two are inelastic processes that change the energy of the scattered photon. Added to this are secondary effects such as the Auger effect, Resonance X-ray Scattering (RIXS) and X-ray Raman scattering (XRS). Inelastic scattering phenomena form the basis of numerous methods of X-ray spectroscopy, such as XPS, Auger spectroscopy, and a number of absorption spectroscopy, which allow to probe the electronic structure of materials. They also provide near-range ordering information, like Extended X-ray Absorption Fine Structure (EXAFS) technique.

The third of the mentioned effects, Rayleigh scattering, is the elastic one, with the scattered photon energy remaining unchanged. Elastic scattering methods include X-ray Diffraction (XRD, MX), the techniques such as Low Angle X-ray Scattering (SAXS), High Angle Scattering (WAXS, at $2\theta > 5^\circ$), as well as Grazing-Incidence X-ray Reflectometry (GIXR) and more. Most of them are widely used in biological research, and the reader will find their more detailed discussions in other available books and articles.

The wavelength range most commonly used in protein crystallography extends from $\approx$ 1.1 nm to $\approx$ 0.05 nm with wavelengths between 0.1 nm and 0.09 nm applied relatively frequently. The photon energy ranges available in a few selected MX lines of European synchrotrons are summarized in Table III. The choice of wavelength is usually linked to the method of solving the phase problem. In the studied protein molecules, the substitution of heavier atoms in place of lighter ones is often used, and then the structure is determined with anomalous diffraction. Then, the diffraction patterns are recorded at wavelengths below and above the absorption edge of the heavy atom. A typical example is the replacement of sulfur atoms with selenium in a common component of proteins — methionine. Selenomethionine (Se-Met or Sem) formed in this way is incorporated in the protein in exchange for methionine. Selenium and sulfur, as adjacent to each other in the group of chalcogens have very similar chemical properties. Therefore, such a replacement usually does not affect the structure

TABLE III

Wavelength/energy ranges of selected MX beamlines at ESRF and diamond storage rings.

Synchrotron	Beamline	Wavelength [nm]	Energy [keV]	Comments
ESRF	ID14 (1–3)	0.093	13.392	fixed wavelength
ESRF	ID29	0.07-0.29	6–20	
ESRF	ID13	0.25–0.073	5–17	optimized for 12.5 keV
diamond	I02	0.25-0.069	5–18	
diamond	I03	0.25–0.054	5–23	
diamond	I04	0.086–0.103 and 0.155–0.190	6.5–8.0 and 12.0–14.5	
diamond	I04-1	0.09163	13.53	fixed wavelength
diamond	I23	0.15–0.4	3.1–8.265	long wavelength MX

and function of the protein. The study of anomalous scattering around the selenium absorption edge has led to *ab initio* solution of many protein structures. The use of selenium as a substituent imposes the diffraction at a wavelength close to 0.098 nm, which defines the position of the K absorption edge of this element. Apart from selenium, atoms of other elements, such as bromine or iodine, can be used as substituents. Also, heavy metal atoms are introduced into the crystal structure (by the method of soaking the crystal, heavy atom Soaks), which are located in specific places of protein molecules. These include lead, platinum (binds to Met, His and Cys), mercury (Cys and His, disulfide bridges), osmium (binds specifically to the 3' end of RNA), rare earths, uranium, and lanthanides (e.g. samarium combines with the phosphates of the protein skeleton), cadmium and the noble gases xenon and krypton, which are deposited in hydrophobic pockets. With the presence of atoms of these elements, it is necessary to use the wavelengths defined by the respective absorption edges for measurement. This can be conveniently achieved with synchrotron radiation by retuning the monochromator.

A detailed discussion of protein diffraction methods is beyond the scope of this study. There are many publications available in this specific and rapidly evolving field of knowledge that may be of interest to the reader, such as by Beis [42], Wlodawer [43], Drenth [44] and many others.

In medicine, the current applications of synchrotron radiation are dominated by scientific research aimed at learning about the phenomena accompanying the physiology of life processes and pathology, and the treatment of diseases. SR sources are especially useful for this kind of application. Increasingly, radiation is also used for medical diagnostics and supports the development of new therapeutic procedures. Apart of a variety of X-ray spectroscopic and imaging methods, the SR diagnostic techniques make use of other subranges of the electromagnetic waves, such as infrared or terahertz microscopies and spectroscopies. Applications of synchrotron radiation in the field of oncological therapy are being developed. Among the most promising methods are here the Microbeam Radiation Therapy (MRT) [45] as well as Photon Activated Radiotherapy (PAT) and Synchrotron Stereotactic Radiation Therapy (SSRT) [46]. In animals MRT has been shown significant advantages in brain tumors. They selectively destroy cancer cells while sparing normal brain cells and connective tissue. This avoids necrosis and preserves the structural integrity of the brain.

Synchrotron radiation offers improved diagnostic methods. Supports the characterization of neoplastic changes of the, among others, skin, brain, kidneys and breast. It helps to understand the mechanisms of cancer spread. For this purpose, a number of spectroscopic and diffraction techniques are used, but the most important application of SR in medical diagnostics is X-ray imaging.

Due to the method of creating contrast, imaging techniques are divided into two main groups: absorption contrast methods, in which the image is formed as a result of local differences in the absorption coefficient of the tested object, and phase-contrast methods, in which the image is formed as a result of local differences in the optical path.

In the X-ray range, the complex refractive index of a material at a given wavelength λ is conveniently represented as $n = 1-\delta+\mathrm{i}\beta$, where the real term δ is a small positive number called decrement of refractive index, and β denotes absorption. The value of δ is proportional to $1/E^2$ (E is the photon energy). In the general case, including materials composed of different types of atoms, the values of δ and β can be obtained with

$$\delta = \frac{R_c\,\lambda^2}{2\pi\,V}\sum_p \left(Z_p + f'_p\right), \tag{1}$$

and

$$\beta = \frac{R_c\,\lambda^2}{2\pi\,V}\sum_p f''_p, \tag{2}$$

where $R_c = 2.82\times10^{-13}$ cm is the classical electron radius, $Z_p + f'_p$ and f''_p are, respectively, the real and imaginary part of the scattering factor of the p-th type of atom.

Note that (1) and (2) are valid if the material density (ρ) is expressed in [g/cm^3] and the wavelength (λ) in [Å]. The relationship between the absorption coefficient μ and β is given by

$$\mu = \frac{4\pi}{\lambda}\,\beta. \tag{3}$$

For high photon energies and far from the absorption edge, the relationships $\delta \propto \lambda^2$ and $\beta \propto \lambda^3$ are approximately satisfied. The expression $N = \delta/(2\pi\beta)$ defines the maximum phase shift in the material due to the reduction by absorption, with $N \propto 1/\lambda$. It reaches higher values for shorter wavelengths [47].

The range of hard radiation up to $\approx$ 30 keV is particularly suitable for phase contrast imaging of biological objects, as its relative sensitivity (defined as $\varepsilon = \delta/\beta$) for a sample composed of light elements is up to several hundred times greater than gives the absorption contrast [48]. In addition the absorption length determines the trade-off between the need to penetrate the sample thickness and the conditions favorable to optimize the dose and resolution. The values of the optical constants for the photon energy range 50 eV–30 keV can be found in the Henke tables [24], and the absorption coefficients for the selected forty substances in the photon energy range 1 keV–20 MeV in Hubble's work [49].

Apart the two basic groups of imaging and microscopy methods mentioned above — absorption and phase contrast — there are also some methods that does not belong to any of these groups. One of them is Coherent Diffraction Imaging (CDI), which uses diffraction of a coherent light beam in microscopic objects that do not need to show periodic order. When applied to biomedical issues, the variant of this imaging method, Coherent X-ray Diffraction imaging (CXDI) using X-rays, is of particular importance. As this method requires highly coherent light sources, we will devote more attention to its properties in the section on free electron lasers.

The range of Hard X-rays up to the limit of Soft X-rays is often used to study the concentration and distribution of trace elements in cells and tissues. The role of trace elements and mineral nutrients cannot be overestimated in the animal and plant world. Each metalloprotein must contain at least one metal atom, without which it will not be able to properly fulfil its vital functions. It is estimated that in the "average" mammalian cell, depending on its function, there may be about 10^9 proteins, some 35% of them being metalloproteins. We can therefore expect that, on average, the number of atoms of all metallic elements in one human cell is, accurately estimated, at least of the order of 10^9. There are certainly many more of them, because, for example, metal ions (sodium and potassium, as well as calcium or magnesium) were not included in this reasoning, circulating relatively freely somewhere in the cytoplasm[†8]. Knowing the volume of such an average cell (it is on the order of 3×10^{-9} cm^3) or its mass (about 3.5×10^{-9} g), and assuming a specific share of atoms of a given element in the estimated number of metal atoms, it is easy to assess the necessary sensitivity of its detection method (we leave this task to those who are interested).

To keep a living organism in a homeostatic condition its cells must contain a complete set of trace elements (not only metals) in certain physiological concentration ranges, depending on the biological species, type of cells and their functions. Data on the role of individual elements and their correct concentrations in organisms of different species are carefully collected and can be found in many textbooks (see, e.g. [50–54]). A kind of periodic table of elements for biology has also been developed, systematizing the occurrence and role of individual elements in organisms. It was applied, among others to explain the "chemical evolution" hypothesis linking the role of trace elements with their presence in the environment [55, 56].

Moving beyond this physiologically useful range of concentration up or down can be a signal that the body is developing some pathological condition that can lead to serious consequences, including death. Hence, determining the concentration of trace elements in cells and tissues of the body and studying their distribution, the dynamics of changes and relationships with metabolic processes is of fundamental importance both for diagnostics and therapy, as well as deepening the knowledge of the physiology and metabolic processes of animals and plants.

In the literature on the subject, there are several dozen laboratory methods for the determination of trace elements. However, if we care about a good resolution (i.e., low detection threshold) and high selectivity of the measurement (both elemental and spatial), the choice is significantly reduced. The detection limits of trace elements and the achievable resolutions of various types of micro-probes clearly indicate the advantage of two measurement techniques (i) proton microprobe (known as PIXE — Particle-Induced X-ray Emission) and (ii) Fluorescent Synchrotron X-ray micro-probe (SRXRF) [57]. In the case of the PIXE/BS method assisted by backscattering (BS) the detection limit was set at 1–10 μg/g and the spatial resolution at 0.2–2 μm. It is a fully quantitative method. The synchrotron fluorescence X-ray micro probe, for comparison, has a detection limit of 0.1 μg/g and a slightly better spatial resolution of up to 0.1 μm.

As in the case of PIXE, the principle of XRF is based on the detection of X-rays emitted from the sample atoms due to excitation with higher energy

[†8]The estimates are based on the data from the book by Ron Milo and Rob Phillips [10], which, can be an excellent introduction to biology for people used to seeing the world through a filter of numerical particulars.

radiation. We will not discuss here the analysis by PIXE, interested readers are referred to the rich literature in this field (see, e.g. [58]). Instead, we will focus on the most advanced synchrotron-enhanced technique today, namely X-ray fluorescence microanalysis, which is multi-elemental and quantitative. The intensity of fluorescence is directly proportional to the concentration of elements in the sample. The analysis of trace metal elements with a high Z value in thin biological samples constituting a matrix composed of light atoms with low Z values is not difficult. There is usually no need to make corrections for the absorption of fluorescent radiation in the sample. However, such a correction must be taken into account when making a quantitative analysis of light elements, usually with $Z \lesssim 17$, lighter than argon.

Third-generation synchrotron sources have been since recently bright enough to generate micro- and nanobeams of sufficiently high intensity to map the distribution of trace elements in biological samples at the scale of a single cell. The optics of X-ray beams with photon energies in the range of soft and hard radiation (from 1 keV up) were significantly improved, achieving a submicron spatial resolution. For instance, the XRF beam available in the ESRF (Grenoble) enables the focusing of photons to the spot size of several dozen nm [59]. Such spatial resolution in combination with high brightness enables imaging of the distribution of chemical elements with subcellular resolution with very high sensitivity in the atto-grams range. Exceptional is the ability to measure in a gas atmosphere. The advantages of the method also include the relatively large penetration depth of X-rays, which allows to study the depth distributions of trace elements without the need for mechanical or ionic interference with the material being tested, close to their natural, hydrated state using dedicated cryogenic methods and without the need of staining.

The use of highly concentrated X-ray beams in the study of biological matter, however, also may have its dark side. High local dose rates generate strong primary and secondary damage to the samples. In addition, a significant portion of free radicals can be generated in air close enough to the sample to contribute to the damaging processes inside it. The stronger the beams are used, the more carefully thought-out and precisely performed the experiment should be. We will pay more attention to the issues of damage later in this work.

2.1.2. Soft X-Ray range (SX), 0.83–24.8 nm, 50–1500 eV

The range of Soft X-rays (SX) is of particular importance for biomedical research. Here, possible is the excitation of electrons in the inner shells of most elements, which is the basis of a number of spectroscopic methods. It includes the so-called water window (shown as W_{SX} in Fig. 2) of wavelengths

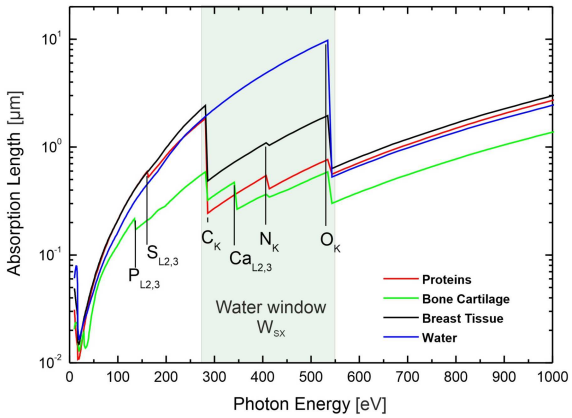

Fig. 3. Soft X-ray water window W_{SX} between the two absorption edges, O_K and C_K, oxygen is almost transparent to radiation, while carbon absorbs strongly. This creates a natural contrast between the water or ice surrounding the biological sample and the carbon included in the structures that make up the cells.

subrange between the absorption edges of oxygen (2.34 nm, 543 eV) and carbon (4.4 nm, 284 eV), characterized by low absorption coefficient of water.

This makes it possible to obtain natural absorption contrast when imaging samples (e.g. tissues or cells), consisting in the differences between a small water absorption coefficient and higher values of this coefficient for substances containing some light elements, such as carbon, nitrogen, calcium or silicon. Apart from its use in X-ray microscopy, it is also important for high-resolution spectroscopy of relatively thick tissue objects and whole cells in an aqueous environment.

The dependence of the absorption length on the photon energy in the spectral range containing the water window for water, proteins and two exemplary tissues are compared in Fig. 3.

The use of phase contrast methods in the SX range is not as effective as in the case of harder radiation due to slight differences in the values of the real part (decrement) and the imaginary optical coefficients (δ/β) for light elements.

2.1.3. The extreme ultraviolet and vacuum ultraviolet (EUV +VUV), 24.8–180 nm, 6.5–50 eV

The extreme ultraviolet and vacuum ultraviolet occupy the band between the Soft X-rays and the optical range. They are characterized by a very high absorption coefficient for most substances, which limits their usefulness to methods of testing geometry and processes in the near-surface part of materials placed in vacuum. Therefore, the EUV and VUV ranges are only sporadically used in the study of biological materials. In the early phase of short-wavelength free electron lasers, when these sources were not able to produce Hard X-rays yet, the XUV

radiation from FELs was successfully used to test the Coherent X-ray Diffraction Imaging technique (CXDI, see Sect. 4.2).

2.1.4. Optical range (UV + VIS + IR), discussed separately

Going up with increasing wavelengths across the subsequent spectral ranges we reach here the non-ionizing part of electromagnetic spectrum.

The photon energy of Non-Ionizing Electromagnetic Radiation (NIER) is insufficient to knock an electron out of an atom or molecule of the in the material with which it interacts. However, the determination of the lower wavelength limit (the upper photon energy limit) for NIER is not obvious, it contains arbitrariness depending on the adopted definition criteria or local habits. It is worth remembering, especially when looking at older works and textbooks.

Among the elements, the lowest ionization energy 3.89 eV (318.73 nm) has been found for cesium [60]. It has been shown, however, that some molecules with closed molecular orbitals exhibit a lower ionization energy (e.g. in the case of $W_2(hpp)_4$ molecule, the ionization energy was determined to be 3.51 eV) [61]. In biological sciences, it is usually assumed that non-ionizing radiation extends from sub-terahertz wavelengths down to 380–320 nm (3.26–3.87 eV), that is up to ultraviolet, above energies of the visible spectrum. Using this convention, it can be seen that the optical range is entirely within the non-ionizing part of the spectrum.

The absorption of tissues and biological substances in the optical range is shaped by the electronic, vibrational and rotational properties of the biomolecules that make up them. For non-turbid materials, the transmittance T is determined by the Beer–Lambert law

$$T = \frac{I}{I_0(1-R_S)} = 10^{-\varepsilon C l} = \exp(\mu_a l), \qquad (4)$$

where R_S defines the specular reflection coefficient for the sample, I and I_0 the intensity of the light passing and incident on the sample, respectively, ε is the extinction coefficient (molar absorption) of the absorbing material, C — its concentration, l — optical path of the light in the absorber, and μ_a is the linear absorption coefficient[†9]. In general, the absorption properties of animal tissues and cells optically are dominated by the absorption of proteins, DNA, hemoglobin, melanin, and water. However, the changes in the absorption properties with the wavelength are different for these substances. This is illustrated in Fig. 4 [62].

[†9]In the field of biomedical optics, the absorption coefficient is usually used to describe the absorptive properties of tissues, while the molar extinction coefficient is used for the properties of individual isolated molecules.

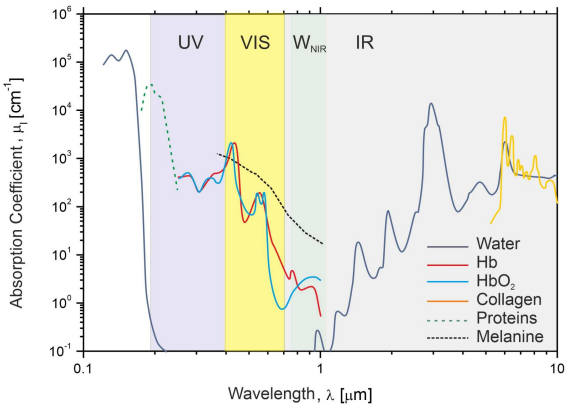

Fig. 4. Absorption coefficients of selected substances and water in the UV, VIS and IR ranges. The so-called near infrared water window W_{NIR} is shown as well (based on [62]).

• *Ultraviolet range (UV), 180–400 nm, 6.5–3.1 eV.* This range has been of interest in photobiology for many years. The energy of the UV photons is high enough to induce transitions between molecular orbitals $n \to \pi^*$ and $\pi \to \pi^*$. The UV range lies entirely in the area of low water absorption, which at shorter wavelengths, below 170 nm, rapidly increases by as much as 6 orders of magnitude. The main absorbents (chromophores) in the UV range among the tissue components are proteins, DNA and melanin. At the smaller UV wavelength, the most important chromophore is the peptide bond (O=C-N-H) present in the backbone of each protein.

Since proteins are one of the most important components in human tissue, right after water, the absorption coefficients of tissues that contain large amounts of collagen (e.g. cornea, skin, connective tissue) are very high in the wavelength range close to 190 nm, reaching μ_a values of the order of 104 cm^{-1}. Subsequently, the peptide bond absorption drops, although still showing significant values up to $\lambda = 240$ nm. At higher wavelengths in the UV range, DNA, aromatic amino acid residues and also melanin become essential chromophores. Both the purine and the pyrimidine bases belong to the aromatic compounds and contribute to the DNA absorption peak at $\lambda = 260$ nm. Due to this peak, the absorption of DNA is 10–20 times higher than that of proteins in the range of $\lambda = 240$–290 nm [63]. In general, the absorption of soft tissues containing high amounts of collagen drops significantly in the UV range with increasing wavelength. Absorption length $(1/\mu_a)$ for these tissues it typically varies from $\lesssim 0.5$ μm at $\lambda = 190$ nm to $\simeq 200$–400 μm at $\lambda = 400$ nm.

Although DNA also shows strong absorption at $\lambda = 210$ nm, its contribution to tissue absorption is negligible compared to the absorption and peptide binding concentration of the proteins present in the tissue. Aromatic amino acids: tryptophan, tyrosine

and phenylalanine also show wide absorption peaks concentrated in the range of λ = 250–280 nm, which are related to transitions between molecular orbitals. However, it should be noted that connective tissue contains relatively few cells and therefore has a low DNA content. Moreover, only 3% of the amino acid residues in collagen are aromatic. Therefore, even in the spectral range, where absorption of both aromatic amino acids and DNA is expected, the absorption of tissues containing mainly collagen is at least 100 times lower at λ = 240–290 nm than in the range of λ = 190 nm.

Melanin absorption is important when considering the absorption properties of pigment-containing tissues such as skin, iris, and the retinal pigment layer. It is worth remembering that the term melanin refers to a broad class of biological pigments whose color in the visible spectrum varies from yellow and red-brown to brown and black. For human skin, the absorption of melanin in the optical range becomes significant at about λ = 300 nm and after reaching a maximum at λ = 335 nm its absorption spectrum declines monotonically with wavelengths from UV to IR.

• *Visible Spectrum (VIS) range, 380–750 nm, 2.75–1.65 eV.* The optical properties of animal tissues in terms of visible light are dominated by the absorption of melanin and hemoglobin[†10]. Hemoglobin always occurs in tissues in two forms: unoxidized (Hb) and oxidized (HbO_2). Although both forms exhibit ultraviolet absorption, this becomes significant only as compared to the absorption of other chromophores in the visible range. Both Hb and HbO_2 have their most pronounced peaks in the violet range, at λ = 433 and 414 nm, respectively. Their absorption drops by over an order of magnitude and then increases again in the green range, where HbO_2 shows peaks at λ = 542 nm and λ = 576 nm, and Hb at λ = 556 nm. The absorption of both of these chromophores drops again by more than an order of magnitude in the yellow and red spectral ranges. Despite the fact that all biomolecules show little absorption in the red and near infrared, both HbO and HbO_2 make a significant contribution to the total absorption of vascularized tissues in the near infrared. In pigmented tissues such as skin, hair and eye tissues, melanin plays a large role in determining the optical absorption properties. The absorption spectrum of melanin is devoid of structure in the visible range, decreasing monotonically with increasing wavelength in such a way that its absorption value at λ = 780 nm is ten times lower than at λ = 400 nm. Such absorption characteristics is quite surprising and can be explained by the fact that this dye is distributed in the tissue in the form of particles (granules) with a diameter of about 150 nm. Thus, the contribution of optical scattering on the particles themselves to the measured melanin extinction coefficient cannot be easily separated from the "pure" absorption of melanin itself. Recent studies indicate that the melanin extinction coefficient is primarily the result of a high value of the scattering coefficient, which dominates absorption more than 100 times.

• *Near and Far Infrared Ranges (NIR + FIR), 780 nm–6 μm and 6–15 μm, 0.21–1.59 eV and 0.083–0.21 eV.* Beside hemoglobin, which contributes significantly to the optical absorption of vascularized tissues down to approximately λ = 1000 nm, the primary infrared chromophores are water and proteins. Water significantly contributes absorption from about $\lambda \gtrsim 900$ nm, becoming the strongest infrared chromophore. Its absorption spectrum is primarily influenced by the resonances of symmetrical and asymmetric stretching modes, which are located respectively at λ = 2.74 μm (ν_1 = 3651 cm^{-1}) and at λ = 2.66 μm (ν_3 = 3755.8 cm^{-1}), as well as resonances symmetrical bending mode at λ = 6.27 μm (ν_2 = 1595 cm^{-1}). These vibration modes and their combinations contribute to the water absorption peaks located at λ = 0.96, 1.44, 1.95, 2.94, 4.68, and 6.1 μm. The optical absorption of water in the near infrared, initially quite weak, increases rapidly with wavelength. In relation to the visible range, this absorption increases by 6 orders of magnitude and reaches its maximum at λ = 2.94 μm, the absorption coefficient is then μ_a = 12 000 cm^{-1}. It is almost three times lower than the optical absorption of collagen-rich tissues in the UV range at λ = 190 nm). The optical absorption of water remains high (μ_a > 500 cm^{-1}) in the far infrared, where there is another maximum at λ = 6.1 μm (μ_a = 2740 cm^{-1}).

The other major chromophores in the IR range are proteins. Protein IR spectra are shaped by the different vibrational modes of the, mentioned earlier, peptide bond (O=C-N-H). The most important of them are (i) stretching C=O, also referred to as the amide-I band, which is for collagen located at λ = 6.02–6.1 μm (1640–1660 cm^{-1}), (ii) coplanar deformation of N-H bond with stretching C-N, defined as amide-II, in collagen at λ = 6.45–6.51 μm (1535–1550 cm^{-1}), and (iii) C-N stretching with coplanar N-H deformation, referred to as amide-III, in collagen at λ = 7.87– 8.13 μm (1230–1270 cm^{-1}). Collagen and water have peaks in the same band at λ = 6.1 μm, where the collagen absorption is more than twice the water absorption. In the range of the amide-II peak at λ = 6.45 μm, the collagen absorption is about six times greater than the water absorption.

The above data relate primarily to animal cells and tissues. In the case of plants, we are dealing with other substances that affect their absorption properties. The absorption bands of the most

[†10]This only applies to those animals that use melanin and hemoglobin. Of course, these are not all animals.

important plant chromophores are in the ranges: chlorophyll-A: 435 nm, 670–680 nm and 740 nm; chlorophyll-B: 480 nm, 650 nm; α-carotene: 420 nm, 440 nm, 470 nm; β-carotene: 425 nm, 450 nm, 480 nm; anthocyanins: 400–550 nm; lutein: 425 nm, 445 nm, 475 nm; violaxanthin: 425 nm, 450 nm, 475 nm. Leaves and other green plant parts usually contain a combination of chromophores. Consequently, their absorption spectra does not show clearly defined peaks. The infrared absorption is generally low, except for the water [64]. Broad absorption peaks are usually visible in the VIS/NIR range at 400–500 nm (anthocyanin absorption), 660–680 nm and 740 nm (chlorophyll absorption), 970 nm and 1450 nm (water absorption) [65]. In plants, apart from absorption, fluorescence is also observed. Chlorophyll fluorescence is directly dependent on photosynthesis. The reflectance of plant parts and animals depends not only on the presence of chromophores but also on the surface structure and the cells themselves. This is especially important in the near-infrared spectral range, where absorption can easily damage the plant. The reflectance of plants is greatly enhanced by scattering on discontinuities in the refractive index of the leaf structure, e.g. at the cell wall boundary ($n = 1.4$) and the intercellular space filled with air ($n = 1$) or water ($n = 1.3$) [66]. Knowledge of these facts is important when designing, carrying out and interpreting the results of experiments with plant material in the optical range of the spectrum.

2.1.5. Terahertz radiation range λ=10–1000 μm, 0.124 eV–1.24 meV, ν=0.3–30 THz[†11]

Both synchrotrons and free electron lasers are sources of strong THz radiation. The absorption in this band results mainly from the rotational movement of electric dipoles in the material. Hence, polar solvents show very high absorption. The absorption of liquid water in the terahertz is also very high (see area D in Fig. 2), with peaks observed at 6 THz and 19.5 THz. However, substances such as ice formed from solidified polar solvents are much more transparent for terahertz because the rotation of the dipoles is strongly limited in this state. The radiation easily penetrates plastic, fibers, ceramics, bricks, non-polar solvents, tissues with a minimum water content (e.g. bones, fat, teeth, tendons). It is impermeable by metals. As the terahertz radiation penetrates many common packaging and clothing made of typical fabrics, it makes it possible hidden hazardous objects to be easily revealed and potentially dangerous materials identified. A number of chemical and biological substances (including bacteria and other pathogens) exhibit characteristic spectral signatures in the THz range, allowing to detect their presence and map their distribution in the sample with a resolution comparable to the wavelength by using spectroscopy and imaging methods. In contrast to penetrating radiation of higher photon energies, the THz photon energies are on the order of a few meV only, far from the ionization thresholds of any materials. Compared to infrared radiation, which also has a high spectral sensitivity to many chemical and biological substances, THz radiation penetrates much more materials [67].

The resonance frequencies of the molecules are within the non-ionizing range. Relatively small biomolecules, such as carbohydrates and many drugs, composed of a dozen or several dozen atoms, show intramolecular vibrational states in the shorter wavelength range, up to the Middle Infrared (MIR). In contrast, the vibrations of macromolecules such as proteins and DNA, composed of thousands of atoms, are in the terahertz range. The use of this part of the spectrum enables therefore spectroscopic examination of changes at the molecular level. Moreover, it is extremely sensitive to the presence of water and changes in the dynamics of molecules.

Many biological materials can be easily identified in the THz range by their refractive index $n(\omega)$. For a given substance, $n(\omega)$ determines the time delay to which the terahertz beam with a given frequency undergoes. This forms the basis of time-domain spectroscopy (THz-TDS).

The far-field imaging resolution is limited by diffraction. Rayleigh's criterion does not allow obtaining a resolution better than $\simeq \lambda/2$). In the THz range, where the wavelengths reach the values of several dozen — several hundred micrometers, the achievable far-field imaging resolution is thus incomparably worse from that in the visible range. To overcome this, it is necessary to apply techniques allowing to bypass the diffraction limit, with aid of the near-field phenomena.

Thanks to imaging in the near-field, using the Scanning Near-Field Optical Microscopy (SNOM) technique, resolutions much lower than the wavelength are achieved. With a variant of SNOM, the so-called Apertureless SNOM (ASNOM), with scattering on the blade and registration by the AFM microscope equipped with the Michelson interferometer, it is possible to achieve a resolution of several to several dozen nm, or even smaller.

SNOM microscopy is often combined with the simultaneous absorption measurement of the imaged material. It has been shown that with this technique (s-SNOM microscopy) spectral "signatures" of viruses on the order of 18 nm can be determined (see Fig. 5 [68], and also [69], pp. 250–253). The amplitude and phase spectra turned out to be surprisingly strong even at volumes as small as 10^{-20} dm^3 for the sizes of the particles and substrate tested. In the case of proteins, this allows the identification

[†11] Formerly called T-rays or submillimeter waves.

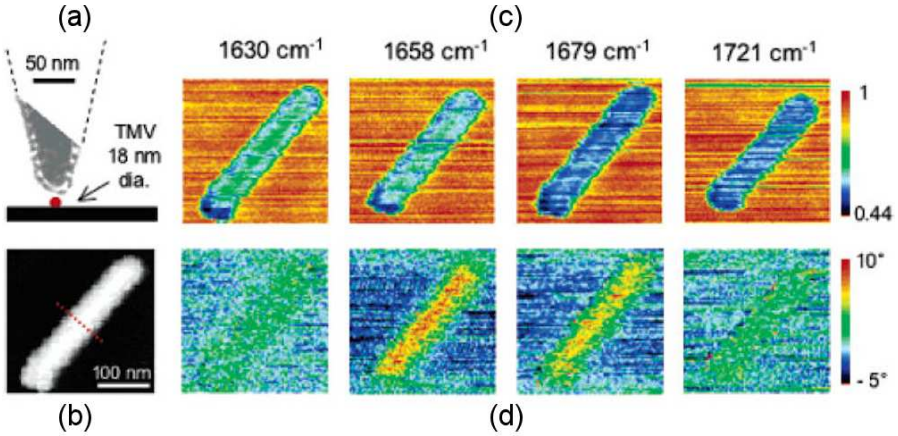

Fig. 5. Single TMV tobacco mosaic virus ($\approx$ 18 nm diameter) on silicon imaged by s-SNOM infrared spectroscopy at different wavelengths. (a) Sketch of the TMV under the probe tip with superimposed (on the same scale) TEM micrograph of the actually used Si tip coated with Pt. In topography (b), the virus appears larger due to its convolution with the tip, which in this case has a radius of $\approx$ 30 nm. (c) Images recorded simultaneously in infrared at different wavelengths, (d) contrast in the near field of the amplitude, respectively, and phases recorded at different frequencies. In the central part of the virus, clearly visible changes in amplitude as well as in phase contrast with respect to the silicon substrate show the same broadening due to convolution (published with permission from [68]).

of the secondary structure. By concentrating terahertz fields to even smaller sizes and using ultrafast high-resolution Scanning Tunneling Microscopy (THz-STM), spatial resolution of $\sim$ 2 nm was recently obtained [70]. The higher the concentration of the beam, the more precise the nanoscopy and the better the detection of a small number of molecules with THz waves.

Due to its properties, terahertz radiation is increasingly used in the field of biomedical sciences. However, until recently, the lack of sufficiently strong, small and cheap sources was an obstacle to the widespread use of spectroscopy and imaging in the THz band on a larger scale. The main applications of these methods include biomedical imaging — safe due to the lack of ionization, in diagnostic situations where relatively small resolutions are sufficient (e.g. pictures of teeth in dentistry, imaging of skin and tissue preparations to detect early pathological changes etc.) [71]. They are also used in protein and DNA spectroscopy [72, 73], measurements of water content in tissues and in food research [74].

It has already been mentioned that the characteristic feature of terahertz and infrared radiation is a small quantum energy, insufficient to break strong chemical bonds, such as covalent bonds. Leaving them intact, however, allows you to selectively break weaker bonds such as hydrogen bonding and Van der Waals [75]. The process of selectively breaking weaker bonds under the influence of THz beam interaction with the material has been called soft ablation or mild ablation. Ablation processes also occur under the influence of infrared radiation in the FIR and MIR ranges, with photon energies higher than THz waves, also non-ionizing. When soft ablation is applied to a large biological molecule, such as a protein or DNA, only weaker bonds defining its conformation are broken, leaving its entire basal sequential structure intact. In many cases, the molecule even retains biological activity. This specific soft ablation is used in modern biological technologies.

THz radiation from a high-power FEL laser in the range of 150 μm induces oscillations of the intermolecular O–H. . . O and O–H. . . N bonds. In this way, a selective dissociation of these bonds occurs and it is possible to transfer the biomacromolecule to the gas phase while maintaining intramolecular covalent bonds. From this phase, they can be transferred and deposited, for example, on a biochip, for further processes. The lack of small-molecule fractions in the size distribution, observed experimentally for macromolecular aerosols, as well as the correlation between the particle size and its molecular weight (for proteins) or the length of the molecule (for DNA) indicate a non-destructive ablation effect when irradiated with 128 μm terahertz waves with THz-FEL laser [76].

Cold vaporization of tissues with a picosecond IR laser or desorption by pulsed excitation of vibrational modes are processes based on an analogous principle. They can be easily excited with a properly tuned THz-FEL beam and successfully applied for example, for the extraction of proteins.

Extracting proteins from tissue is a key step in the sequence of proteomic research procedures. As cell membranes are destroyed during conventional mechanical homogenization, various enzymes are released that can degrade and transform other proteins. As a result, during mechanical homogenization, the original molecular composition

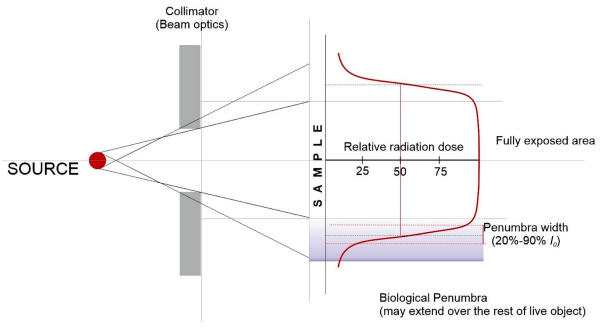

Fig. 6. The zones of interaction of radiation with the tested object. Incident beam angle and source size are significantly exaggerated. In practice, even in the case of focusing with X-ray mirrors, the aperture/convergence angles of the beam do not exceed a few degrees. In addition to the penumbra, distinguished is also a zone of biological penumbra, associated with disorders outside the proper area of irradiation, induced by intra- and inter-cellular mechanisms by radiation damage. It can extend even over the whole organism.

changes in vitro, resulting in a false image of the proteome. Using a Picosecond Infrared Laser (PIRL), the tissue can be vaporized and homogenized in seconds. In an almost homogeneous tissue aerosol, proteins dissolve. It has been shown that although the PIRL method causes increased proteolysis, the molecular composition of the proteins extracted from the tissue with PIRL is closer to the original composition *in vivo*, the enzymatic degradation is lower, and the process efficiency is higher compared to classical extraction methods [77, 78].

3. Radiation damage

Radiation damage is an inevitable consequence of the interaction of radiation with matter.

From the point of view of the damage mechanisms generated in the sample by the photon beam, the entire spectrum of electromagnetic radiation can be divided into two parts. Namely, the range of ionizing radiation, with photon energy higher than a few eV, sufficient to eject the electron out of the atom, in solids into a continuum of states, and the range of non-ionizing radiation in which the photon energies are too small to do this, but they can excite electrons to higher, unoccupied energy states.

For all materials, wavelengths and beam intensities, an important issue is the influence of radiation on the sensitivity, the spatial and temporal resolution of the measurement, as well as on the durability of irradiated material. It should be kept in mind that during the measurement the test object can be changed by interaction with the radiation beam. As a result, its structure and function may be destroyed, or heavily affected by the irradiation defects or, apart a phase transition, some chemical reactions can be initialized by free radicals or photons etc. Any methods using high-intensity synchrotron radiation beams must take into account the radiation damage as an inherent part of the experiment (see Fig. 6).

The concept of radiation damage is most often used in a narrow sense, only in the case of damage caused by ionizing radiation. In a broader sense, it also refers to damage or modifications generated by non-ionizing radiation, e.g. visible or infrared, which, due to absorption in the material, may lead to changes in some of its functions due to the initiation of chemical photoreaction by photons, thermal damage, and even, with sufficient high fluence, ablation. It also includes intermediate cases with photon energies close to but below ionization thresholds. Detailed studies of the mechanisms and the real significance of these low-energy damage have only recently been developed.

In this paragraph, we will primarily deal with radiation damage in the narrower sense, generated by ionizing radiation.

The dose energy deposition (E_d) [J/kg] is defined as the amount of ionizing radiation energy absorbed by the sample per unit mass, i.e.,

$$E_d = E_i \frac{\mu_e}{\rho}, \tag{5}$$

where E_i is the energy of radiation incident on the sample. It is defined by

$$E_i = k\, t\, E \frac{I}{A}. \tag{6}$$

Here, $k = 1.6 \times 10^{-19}$ J/eV, E— photon energy [eV], t — exposition time [s], I/A — fluence [photons/(s mm^2)], μ_e/ρ — mass absorption coefficient. The SI unit of absorbed dose is Gray [Gy] (1 Gy = 1 J/kg).

It is a measure of the amount of energy absorbed by a given object per unit of its mass. Protein crystals during structure examination by X-rays typically receive millions of Gy, so MGy is a more practical unit, at least in protein crystallography. The flux densities (expressed in the number of photons/(s μm^2) of today's X-ray synchrotron beams may differ by four or more orders of magnitude [79]. The amount of radiation damage depends on the number of absorbed photons. Not the total energy of interacting photons count, only truly absorbed fraction of this energy, responsible for triggering processes leading to destruction [80, 81]. Therefore, it is appropriate and useful to describe the damage in terms of dose. Note that the fluence (photons incident on the μm^2 of sample surface, or energy which they carry) is sometimes incorrectly referred to as dose. The definition of dose means absorbed energy, not incident energy or number of photons. For Hard X-rays this is met up to a certain limit of photon flux density, which was estimated as not lower than 3×10^{15} photons/(s mm^2) [82]. For higher flux densities, dose-dependent nonlinear effects begin to play a role, resulting in sample structure destruction.

Radiation damage to biological objects has particularly serious consequences. For methods used on living organisms or their parts (e.g. tissue cultures), the acceptable level of irradiation is far lower compared to that of most solid inorganic materials.

We must distinguish between two basic cases. The one refers to the in vitro testing of biological, cellular and tissue preparations or biomolecules, e.g. in the form of a suspension, protein crystal or isolated, with the use of synchrotron radiation beams. The other relates to the *in vivo* interaction of beams with living multicellular organisms, like highly organized Chordata, Vertebrates, Mammals, including humans. The accumulation of radiation damage in the tissues of living organisms is not only able to significantly change the structure, chemical composition or morphology of objects. Usually, the vital functions are impaired earlier, which in turn may lead eventually to the death of the whole organism, even many days after irradiation. Here, the admissible radiation doses are incomparably lower than in the first case. Except in very strictly defined and justified cases, they must not be exceeded, if we are to avoid serious health complications of the organisms being examined with radiation[†12].

For obvious reasons, during *in vivo* tests, some commonly used methods of limiting radiation damage that could stop life processes or disrupt the studied process, e.g. cooling to nitrogen temperatures, cannot be used either. It should be emphasized that the influence of ionizing radiation on living organisms is not limited to the directly absorbed dose. The chemical interaction of reactive compounds and free radicals generated by the synchrotron beam in the medium surrounding a living organism (usually water or air) is also important. They can enter the body/cells, for example through breathing or directly through skin, and induce there significant damage.

With the advent of the 3rd and recently 4th generation SR sources[†13], the interest in the issue of radiation damage induced by intense synchrotron beams has increased again [83–85]. Initially, a higher prevalence of radiation damage was reported which was attributed to the higher beam fluences. However, in tightly controlled experiments, no significant increase in damage was observed with the dose rate. It was also feared that the high intensity of the radiation would heat the elements in contact with the beam, which would indirectly lead to heating the sample itself. But it has been experimentally shown by using the strongest sources that this effect is barely visible (at least in the case of protein crystallography). On the other hand, since it is possible to deliver a certain dose in a shorter time with a more intense beam, then the heat dissipation rate might be insufficient.

It seems that a significant part of these discrepancies can be explained by inadequate dose control and, mentioned elsewhere in Sect. 3, the influence of ionization not of the sample itself but of its environment. This effect should always be considered when working with intense synchrotron sources and samples placed in the air or in water. Especially when using a feeder (dispenser) containing many samples placed near the synchrotron beam. The total time of exposure to damage due to e.g. ionized air may then be equal to the sum of the open beam time for testing all samples. To minimize the impact of this factor, it is worth, for example, to ensure air exchange in the vicinity of the samples and to design the experiment in such a way that they are stored in a zone isolated from the migration of free radicals, from the vicinity of the beam.

Special attention should also be paid to the adjustment procedure of the samples in the X-ray beam before the actual measurement. The time of such operations should be minimized, and the beam itself should be weakened to the necessary minimum level, e.g. by applying attenuators of the incident beam. The attenuators should be placed, preferably, before the beam enters the hutch. If possible, make adjustments with a closed beam using, e.g. calibrated optical position markers or use a substitute sample. Note: when strong additional light sources, e.g. optical lasers, are used for adjustment, it is worth checking that the sample does not degrade under their influence.

The issue of radiation damage becomes qualitatively different in the case of the strongest sources of ionizing synchrotron radiation, i.e., short-wave free electron lasers. We will touch upon this issue in Sect. 4.

3.1. Radiation damage to biomolecules

Ionizing radiation damages all biomolecules in a similar way, including also DNA and RNA. Bonds breakings and other types of damage occur directly as a result of the ionization of the molecule (or atom) itself and indirectly through the ionization of the molecules surrounding the biomolecule (mainly water) and the destructive effect of the reactive particles formed as a result. The most important of them are the free radicals: the hydroperoxide radical, the hydroxyl radical and the superoxide anion radical. Some simple chemicals massively generated during irradiation can cause a great deal of damage. In addition to the H_2O_2 (responsible for $\frac{2}{3}$ of all biological damage), here are also atomic oxygen O,

[†12] One of such cases is, for example, the Microbeam Radiation Therapy (MRT) of neoplastic tumors, developed on synchrotrons, in which the therapeutic doses of radiation exceed many times the doses allowed in classic radiotherapy.

[†13] The 4th generation light sources are called sources whose at least one of the important parameters characterizing the beam, such as brightness, emittance, coherence or pulse length, is at least 1–2 orders of magnitude higher than in 3rd generation sources. Previously, the term was used to describe shortwave FELs. Recently, synchrotrons of the newest design (e.g. MAX IV) have been identified in this way.

TABLE IV

Biomolecular crystals. Typical destructive doses in Gy (DD) for various techniques and radiation sources. Here, MX — macromolecular crystallography, SFX — serial crystallography, RT — room temperature, SR — synchrotron radiation from storage ring.

Technique	Source	DD [Gy]	Comments
MX	SR X-ray tubes	5×10^5	crystals @RT [11]
MX	SR	3×10^7	crystals @77–100 K
MX	SR	$\sim 3 \times 10^7$	crystals @RT [12]
			exposition < 100 ms
Bacteriorhodopsin, MX	SR, X-ray tubes	6×10^5	crystals @100 K [13]
			(beginning of struct. changes)
SAXS	SR	4×10^2	@RT [14]
SAXS	SR	1×10^8	@100 K [15]
SFX	XFEL, fs pulses	$3–7 \times 10^8$	single crystals, 0.1–1 μm
single molecule diffraction	XFEL, fs pulses	1×10^9	(anticipated) single pulse

and ozone O_3. The direct damage mechanisms include both the bond breaking as a result of interaction with the primary photon or inelastically scattered photon, as well as the damage induced by ionization cascade of the photoelectrons and Auger electrons produced by primary ionization.

The types of damage depend on the chemical bonds that make up the molecule. In the case of proteins, the S–S bonds are most vulnerable to damage, as well as those of carboxyl groups and other charged residues. Breaking the bonds leads to many other effects, such as changing the local charge of the molecule and its environment, or conformation modifications.

Radiation damage is not local. Although the primary ionization takes place on a specific, spatially located atom, the energy deposited as a result of it, is rapidly relocated with the ejected photoelectrons and Auger electrons. For example, photoelectrons created by interaction with a biological sample of a photon of energy 12.4 keV ($\lambda = 0.1$ nm), transfer $\sim 95\%$ of the absorbed photon energy, on average, over a distance of ~ 2.8 μm. Their energy is shed in the next acts of ionization, generating cascade of damage. For each act of inelastic scattering on successive atoms, there is an average of a dozen or several dozen eV of energy lost, the rest is sufficient to generate subsequent ionizations. On average, only 5% of the photon energy remains absorbed within a radius of 0.5 nm from the first interaction site. Secondary radiation damage is also delocalized. The migration of free radicals can take place over much greater distances, and its speed and extent depend on the temperature, chemical composition and structure of the sample. Thus, radiation damage also affects non-irradiated areas.

3.2. Radiation damage to biomolecular crystals

In addition to the radiation damage discussed earlier, other specific damage is observed in protein crystals. These include, among others, reduction of metallic centers, increase in unit cell volume and lattice parameter due to accumulation of damage, decrease in the intensity of diffraction peaks, as well as increase in the value of the temperature factor.

The resolution of X-ray diffraction and imaging methods is fundamentally limited by radiation damage. In the case of imaging the aperiodic objects, e.g. using one of the X-ray microscopy methods, the tested samples are usually destroyed by irradiation before the registered number of photons allows obtaining an image with a resolution comparable to the wavelength. In the case of classical X-ray diffraction, this difficulty is avoided due to the multiplication of the "research object" — the unit cell — in the periodic crystal structure. With a sufficiently large crystal, it becomes possible to recreate the spatial arrangement of the base atoms. For a given protein crystal and radiation wavelength, the minimum size necessary to fully recreate the structure with a given spatial resolution can in principle be determined. J.M. Holton and K.A. Frankel [86] estimated that for a spherical lysozyme crystal the smallest size is of 1.2 μm, assuming ideal measurement experimental conditions, that is an excellent diffractometer, a stable beam in a time and space, the use of an excellent detector with a large acceptance angle and for measurements in vacuum. It is worth emphasizing that this is a theoretical limit. In practice, the crystal should be 2–4 orders of magnitude larger in volume to be fully structurally characterized with atomic resolution. In the case of a hen egg lysozyme crystal with a tetragonal structure (unit cell volume $= 239.2$ nm^3), this corresponds to $\approx 10^{10}$–10^{11} unit cells and gives a result similar to the older calculations using the Monte Carlo method and experimental data showing that to obtain minimum good quality diffraction data, the crystal volume should range from about 15 μm^3 to about 35 μm^3 [82, 87]. These values should also be considered indicative (see Table IV). The differences in estimating the minimum size result primarily from the use of different assumptions as to the resolution and the acceptable damage limit.

For further information on the basic mechanisms of radiation damage to the crystals of proteins can be found in many works devoted to the use of X-rays, including SR produced from sources in protein crystallography. For example, it is worth taking a look in a practical guide to radiation damage in protein crystallography published by J.M. Holton [88] and in a concise review by M. Jaskólski on structural studies of biological macromolecules [34].

3.3. Radiation damage to DNA

DNA integrity is critical to life processes. Due to the importance of both radiological protection of living organisms and the optimization of radiotherapy, radiation damage to DNA and its impact on the functioning of the entire organism have been the subject of extensive research for decades. Depending on DNA damage locus, there are distinguished four principal types of damage. The damage to the base (base damage), attachment of an external protein to the DNA (DNA-protein crosslinks), single-strand helix breakage (SSB, Single-Strand Break) and both strands break (DSB, Double-Strand Break). Among the latter, there are also distinguished close and distant breaks, based on the distance between damage on individual strands. The description of the entire complexity of the radiation damage processes mentioned here is beyond the scope of this study. The interested reader may find more detailed information on this in numerous original works, including [89–96] and references therein.

Electrons of energy below 15 eV can attach directly to the molecule, creating "resonances". It has been shown that this can lead to the formation of SSB and DSB damage in DNA even at electron energies of the order of 3 eV [97]. This finding contradicts the traditional view that DNA damage can only be induced by secondary electrons that have energy above the ionization threshold. It also brings new light to the issue of genotoxicity of radiation with relatively low photon energies in the UV–VIS range.

Radiation damage to DNA has three possible consequences for the cell:

(i) successful repair whereby the cell can continue to function fully;

(ii) ineffective repair that could cause the cell to die or mutate; Some of these mutations may lead to pathological cells, including neoplastic transformation.

(iii) the cell cannot be repaired. This leads to its death.

Cell death can occur through one of several mechanisms. One of them is apoptosis, found in multicellular organisms. It is an organized process of killing a cell by contracting as it loses water. There are two possible variants of apoptosis early (applies, for example, lymphocytes) and delayed. Intense apoptosis is usually related to the organism's sensitivity to ionizing radiation. Unlike apoptosis, death by necrosis occurs as a result of autolysis by its own enzymes and is not controlled by cellular or tissue mechanisms. In this process, there is a gradual degradation of cell structures caused by chaotic processes inside the cell, e.g. protein denaturation, membrane decay, and disorganization of signaling pathways. In contrast to apoptosis, the contents of necrotic cells leak out into the intercellular space. Another common mechanism of cell death from radiation damage is delayed death during mitosis. It can take place even a few or a dozen cycles after irradiation (two types: mitotic catastrophe, abortive mitosis). Yet another mechanism relies on the acceleration of the aging process of the cell leading to its faster death.

3.4. Species and tissue aspects of radiation damage

The susceptibility of living organisms to radiation damage depends on many factors, such as the size and redundancy of the genome, the ability to repair, the water and oxygen content in the DNA vicinity as well as, for example, the telomere length [98]. In general, mammalian cells are much more susceptible to radiation damage than microbial cells. The limit dose administered at one time to the whole body, after which 50% of individuals die, is about 3.5 Gy for dogs, about 5 Gy for humans, for rats, mice and rabbits about 8–9 Gy. For cockroaches, similarly to *E. Coli* bacteria, the limit dose is ≈ 7 times higher (60–64 Gy). Yeast can withstand doses of $\approx$ 450–500 Gy, *Drosophila melanogaster* slightly higher, up to 640 Gy, while the structure of the potato blight agent "survives" doses several times higher.

The term IRRO (Ionizing Radiation Resistant Organisms) defines organisms for which the dose of ionizing radiation resulting in a 90% reduction in the population (D10) exceeds 1000 Gy. These include:

- amoebas (rootstocks, over 1000 Gy),
- some primitive wasps from the *Braconidae* family, especially the species *Habrobracon hebetor*, 1800 Gy, (but sterility develops from a dose of $\approx$ 50 Gy [99]),
- tardigrades (*Tardigrada* — a type of microscopic invertebrate animals), especially the species *Milnesium tardigradum*, in which exceptional resistance to irradiation (lethal dose of about 5 kGy, but becoming sterile after taking a dose of 1 kGy) was only recently discovered [100].

The highest resistance to ionizing radiation so far has been found in the bacteria *Deinococcus radiodurans* (15 kGy), and in the archaea's extremophile *Thermococcus gammatolerans*, for which the lethal dose was set at 30 kGy [101].

More and more data testify to the anomalous effects that arise in living tissues even at very low doses of ionizing radiation. Three phenomena are

mentioned here: low dose hypersensitivity, adaptive response and bystander effect [102–104]. The low dose hypersensitivity manifests in an unexpectedly large biological response to small single doses of radiation, characteristic of significantly higher doses. The adaptive response is based on increased resistance to radiation applied in subsequent doses acquired as a result of irradiation with the first, small dose. The bystander effect causes directly non-irradiated cells to be affected by the indirect effects of irradiation. Partly responsible for this is the diffusion of reactive particles resulting from secondary radiation damage. However, an important role plays here the contact of neighboring irradiated and intact cells (in terms of information and biological material exchange), which may also result in a significantly increased resistance of the tissue to the effects of irradiation. The bystander effect is presumed to play a fundamental role in the accompanying mechanisms of synchrotron Microbeam Radiation Therapy (MRT). Such phenomena depend on the type of cells, radiation dose, method of its administration and a number of other physicochemical factors, the role of which in these processes is not yet well understood. These unexplored phenomena may carry important implications for understanding and predicting the biological effects of irradiation beyond small doses.

3.5. Methods of reducing radiation damage

As already mentioned, radiation damage is an inherent part of any experiment involving the irradiation of a sample with ionizing radiation. A well-known method of reducing the rate of accumulation of radiation damage is to cool the sample down to cryogenic temperatures. It is only effective against secondary damage processes. Low temperature slows down the diffusion of reactive particles, mainly free radicals and water radiolysis products, created as a result of interaction with radiation, and decreases the rates of reactions inducing further damage by these particles. By cooling the protein crystal to 100 K, the secondary damage practically ceases to spread. As a result, the radiation tolerance of the crystal (dose tolerance) improves and its "survivability" increases about 50–100 times compared to the samples irradiated at room temperature. It has been shown that the maximum dose of radiation for protein crystals cooled to 77 K (nitrogen boiling temprature), subjected to diffraction is about 35 MGy. Sometimes a similar dose value is given, at which the intensity of diffraction peaks drops to half, $I_{\frac{1}{2}}$ dose $= 4 \times 10^7$ Gy. Further cooling down to the temperature of liquid helium does not significantly change this value, which confirms that already at temperature of 100 K practically all reactive radicals are "frozen" [105, 106].

The dose absorbed depends also on the crystal thickness. For very thin crystals it is significantly lower [107]. This phenomenon results directly from the previously mentioned non-locality of the radiation damage. As it was mentioned earlier, when a radiation damage act is induced by direct interaction with a photon or with the emitted photoelectron, then the absorbed energy usually sufficient for many further interactions is carried by subsequent inelastically scattered photons, photoelectrons and Auger electrons, spreading in the crystal for a distance of several micrometers. For crystals of comparable size, some part of this energy may "leave" the crystal together with these quanta or electrons, thus it will not participate in further damage to the crystal. However, crystal shrinkage cannot be continued arbitrarily because the amount of elastically scattered photons contributing to the diffraction peaks will also decrease.

Still an underrated factor influencing the size of the dose is the careful planning of the experiment in terms of radiology. This allows to minimize the absorbed dose to the level necessary to achieve the precision determined by the photon statistics. The profligate use of the available photon flux is characteristic especially for users of 3rd generation sources, which may result in excessive exposure of samples to unnecessary irradiation. The use of dose calculation software helps to optimize exposure. One of the most widespread, not only in the community of protein crystallographers, is the RADDOSE program created by J.W. Murray [108, 109], then modified by K.S. Paithankar [110, 111]. It allows to simulate a one-dimensional model of the absorbed radiation dose in the case of a stationary (non-rotating) macromolecular crystal and to determine, i.e., its survival time in a given beam by comparing it with the experimentally determined dose limit. It is assumed that the crystal is completely illuminated by a homogeneous X-ray beam. Thanks to this, it is possible to predict, for example, the exposition time after which the crystal will absorb the irradiation dose that makes crystal damaged to the level excluding of further diffraction pattern recordiong, under given experimental conditions and, accordingly, design the experiment using other software, like BEST, to optimize the measurement [112].

The increasing demand for the study of molecular crystals with intense microbeams of sizes ranging from hundreds nm to 20–30 μm has led to development of new dose modeling software due to the fact that the micro-beams are generally of highly inhomogeneous intensity distributions. As a result, a new version of the RADDOSE-3D code was created, allowing for three-dimensional determination of the dose distribution in the investigated crystal [113–116]. Access to the RADDOSE-3D software can be found on the website [117].

Lowering the background recorded by the detectors is not always appreciated measure improving the statistics of counts. This is achieved by reducing scattering on the materials surrounding the sample (including shortening the beam path in air), avoiding large Z atoms in the beam path, especially in the

sample holder, clean and quick freezing, preventing the formation of large ice crystals. Instead of nitrogen, low atomic helium vapors can be used for cooling, which reduces scattering in the beam region and thus reduces the background detected by the detector. The reduction of the radiation dose is also influenced by the use of appropriate recording electronics with detectors with the largest possible dynamic range of counts and the lowest noise-to-signal ratio. The shortest possible reading time is also important. As the detector usually does not register photons during reading and the beam is on, it increases the level of radiation damage "unproductively". For example, if the detector reads every 1 s, and the reading time is 100 ms, it means that as much as 10% of the absorbed dose "works" only on radiation damage.

Often, it is not possible to cool the tested samples down to the boiling point of nitrogen, which is accompanied by solidification of the water with all the consequences that this fact has for the tested material. In such cases, the impact of secondary radiation damage cannot be avoided, but only mitigated. Unlike primary damage, which is dose-dependent only, this type of damage is also time and temperature-dependent. One of the worth considering experimental strategies for reducing damage may be to increase the irradiance and shorten the exposure. In the case of some biological preparations, it is also worth considering the use of cryoprotectants that allow for lowering the freezing temperature of the sample. However, the use of such methods is limited and will not be discussed further here.

The use of monochromatic radiation where possible is the primary method of reducing radiation damage, for example in medical X-ray imaging by absorbent contrast methods. Monochrome X-ray beams avoid the so-called hardening effect. It is based on the increased absorption of the soft radiation components of the polychromatic beam in the sample volume as compared to the components with a shorter wavelength. Due to the relatively higher absorption, lower energy photons contribute less to image formation (the so-called "dose without information"). In turn, high-energy photons contribute to image contrast degradation due to increased scattering. In the case of mammography, it has been shown that the use of monochromatic synchrotron radiation with photon energy in the range of 17–33 keV significantly reduces the radiation dose during image formation, which is characterized by higher contrast and resolution compared to the results obtained with devices using filtered X-ray radiation from a classic tube to mammography.

4. Free electron lasers and their applications in biology and medicine

Today, the most advanced radiation sources are free electron lasers FEL. In a nutshell, these devices are a combination of a relativistic electron

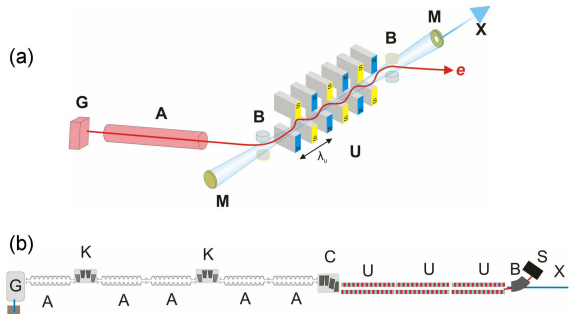

Fig. 7. (a) Diagram of a low gain FEL with a resonant cavity. Emission range: FIR-UV. (b) High gain SASE–FEL design diagram operating without a resonant cavity. Emission range: (FIR)–EUV–HX. Description: G — electron gun, A — electron accelerator modules, U — undulator section, B — bending magnet, M — resonance cavity mirrors, S — electron beam absorber, X — output beam, K — electron beam compressor (Chicane), C — electron beam collimator [118].

accelerator (usually a linac, often superconducting) and an undulator. The basic properties of FEL radiation and optical lasers are similar to each other, but the principle of generating a light pulse is quite different in these devices. In the case of FEL, the role of the active medium and the energy pumping process are taken over by relativistic packages of free (unbound) electrons. Due to the fact, that conversion of electron beam energy to radiation occurs in an alternate magnetic field inside undulator, the FELs are included in the synchrotron radiation sources.

The wavelength of the light emitted by the FEL λ_{ph} determines, as for the undulator, the relationship

$$\lambda_{\mathrm{ph}} = \frac{\lambda_{\mathrm{u}}}{2\pi}\left[1 + \left(\frac{e}{2\pi}\frac{B_{\mathrm{u}}\lambda_{\mathrm{u}}}{m_e c}\right)^2\right], \tag{7}$$

where

$$\frac{1}{\gamma} = \frac{m_e c^2}{E_e}. \tag{8}$$

Here, e is the electron charge, m_e is the electron rest mass, E_e is the electron energy, λ_{u} is the undulator magnetic period, and B_{u} is the magnetic field inside the undulator.

As one can see, λ_{ph} depends only on the last three quantities. This means that the wavelength emitted by the FEL can be easily tuned continuously by changing, for example, E_e.

There are two basic types of free electron laser. The historically first FEL, constructed in 1976 by John Madey [119–122], is a low gain FEL. In order to induce a laser action, it is necessary in this type of device, as in the case of traditional lasers, to use an optical resonance cavity by use of a semi-transparent mirror (see Fig. 7). It limits the energy range of the emitted photons to the Vacuum

Ultraviolet (VUV), as there are not known materials for the mirrors operating at higher photon energies. Sources of this type are mostly used in the ranges of infrared and terahertz radiation.

The other type of FEL uses the Self-Amplified Spontaneous Emission (SASE) process, and does not require a resonant cavity. Due to this, and also thanks to the use of a special structure of the electron accelerator together with optics shaping the electron beam, SASE–FELs are able to produce light also in the spectral range from Vacuum Ultraviolet (VUV) to Hard X-rays in the form of intense pulses of duration of the order of 10–100 fs, shorter than the time constants of most processes related to the change of atomic structure and energy transport. This radiation is monochromatic, fully polarized, with a high coherence and collimation. The peak power emission per pulse can exceed 15 GW, and the radiation intensity values achieved today by focusing, reach up to 10^{20} W/cm^2. The spectral brightness of these sources is more than 8 orders of magnitude higher than the brightest known X-ray SR sources of 3rd generation. Single focused pulses are able to induce ablation in each material and allow for the excitation of extreme states of matter, including the state of the so-called warm dense plasma. SASE–FELs create a new class of synchrotron radiation sources[†14].

This particular combination of parameters has opened up ways to the development of new methods of studying the structure and dynamics of condensed matter processes with unprecedented sensitivity, temporal and spatial resolution, unattainable using other known sources. For life sciences, this presents the prospect of a revolution leading to a deeper understanding of the foundations of life and details of multitude of its processes.

Detailed descriptions of the principle of operation, an overview of the properties of free electron lasers and the research carried out with them can be found in many papers (e.g. [123–127]). In Sect. 4.1, we will discuss, for example, some of the growing applications of FEL in biology and medicine.

4.1. Applications of FEL for tissue ablation

One of the first issues for which low-gain FEL operating in the infrared range was used at the end of the last century was the interaction of intense laser beams with tissues. New monochromatic sources with their tunable, high intensity and controlled temporal pulse structure significantly contributed to the development of biomedical laser techniques, facilitating the systematic work on optimizing the ablation parameters. The mechanisms and effects of ablation as a function of dose, wavelength, energy and time structure of impulses for various types of tissues were investigated [128].

Optimal laser tissue ablation may be highly efficient with the lowest possible side effects. The most important are here the irreversible damage to the surrounding tissues accompanying the ablation and the overheating of the tissues in the more distant zone. The basic parameters optimizing the ablation process include the selection of the wavelength at which the radiation has the lowest possible penetration depth in the tissue. This increases the density of the deposited energy and allows the process to be limited to small volumes (depths). The optimal wavelength depends primarily on the relative (differential) absorption of the main components of the tissue, which are usually water (brine–saline), specific proteins and, in the case of certain tissues, such as bone, minerals. It is equally important to thermally isolate the irradiated volume so as to limit the spatial range of thermal diffusion from this volume, and thus the temperature growth around it. At the same time, the extent of the stress field should be limited, which leads to an increase in the efficiency of the ablation process. It has been experimentally confirmed that this results in a reduction of the volumetric energy density needed for the ablative removal of the material. A review of these issues can be found, for example, in the work of Edwards [129] and references therein.

Based on the tissue's absorption spectrum, it is usually possible to typify certain wavelengths associated with characteristic peaks in the absorption spectrum as potentially optimal for ablation. However, the real complexity of the processes of energy absorption and transport accompanying photoablation of a specific type of tissue requires the selection of all relevant parameters through experiment. Using the IR–FEL laser in the wavelength range 1–10 μm (NIR and mid-IR), several characteristic absorption bands potentially important for ablation optimization were identified in various tissues. These include:

- water (OH, stretching mode), 2.94 μm, proteins (amide-II band), 6.45 μm, and
- (C=O, stretching), 8.525 μm, water (HOH, bending), and
- proteins (amide-I), 6.10–6.12 μm, cholesterol (CO, stretching), 7.01 μm, (POP, antisymmetric stretching), 8.17 μm.

Much attention has been paid to investigating the mechanisms of ablation and peri-ablative damage which depend on both the wavelength and the temporal structure and energy of the pulses. Dependence on the wavelength is related to the competition of two dynamic processes accompanying ablation, i.e., explosive evaporation of brine and the denaturation of specific proteins of the tissue structure [128, 130, 131].

[†14]SASE–FEL lasers emitting in the XUV and X-ray ranges are often incorrectly considered to be the only representatives of free electron lasers.

Surgical ablation of specific hard and soft tissues was also studied at different wavelengths, determining in many cases the optimal process parameters. For cortical bone, optimal ablation was achieved at 6.1 μm [132]. Optimal wavelengths for laser treatment of root surface caries were determined to be 9.0 μm and close to 9.7 μm, which corresponds to the absorption peak due to stretching of P-O bonds in dentine [133]. Efficiency and parameters of ablation of eye tissues and nervous tissue, as well as photothermolysis of lipid-rich tissues were also studied. Cerebral ablation experiments carried out on the rat brains allowed to determine the optimal wavelengths in the mid-IR range for neurosurgical procedures [129].

To test the real possibilities of IR–FEL lasers in surgical practice, a limited number of human surgical procedures were performed. For this purpose, an operating room was built at the FEL center of Vanderbilt University in Nashville. The FEL laser operating in the mid-Infrared Range (MIR) has been successfully used in neurosurgical, oncological and ophthalmic operations [134–136].

Few of the experiments focused on surgical photoablation were also carried out in the UV and VUV range with the FEL OK-4 laser at Duke Durham University (NC, USA) using the storage ring to accelerate electrons to 750 MeV. This allows to obtain radiation beams with a wavelength up to 217 nm [137]. It should be emphasized, however, that research in the area of shorter wavelengths is in its infancy. Irradiation with photons of energies inducing ionization in tissues leads to specific ablation mechanisms with a significant share of radiation damage caused by ionizing radiation. The advantage of higher photon energies is that they are capable to break directly strong chemical bonds. The dissimilarity of the damage mechanisms is also influenced by a different dependence of the radiation absorption coefficient in the material, which results in separate deposition and dissipation processes of the pulse energy in the tissues.

A significant obstacle faced by the implementation of conventional optical lasers in surgery, especially in neurosurgery, is the tissue diversity of the operating field. It causes difficulties in selecting and tuning the laser to the locally optimal wavelength and other ablation parameters. In neurosurgical procedures, this results in unpredictable effects on surrounding tissue structures, such as in deeper areas of the brain or in the cranial nerves. Another problem is the dependence of the effects of laser cutting on the degree of tissue vascularization. Thus, for example, in areas of the brain vascularized more densely (the cerebral cortex) and less frequently (white matter), laser ablation occurs differently. In addition, the effect of carbonization of the nervous tissue accompanying ablation hinders and slows down laser scalpel treatments.

An ideal laser as an instrument for neurosurgery must be a perfect, highly precise "bloodless scalpel" that allows selective removal of only pathological tissues (e.g. a tumor). The most common brain tumors grow into adjacent tissues in such a way that their complete removal by conventional neurosurgical techniques is often not possible. Due to their unique properties, free electron lasers can make a significant contribution to the detailed understanding of the mechanisms of tissue damage and ablation and their dependence on beam parameters, such as wavelength, fluence, and pulse length and temporal structure. As a consequence, new, optimized laser surgery techniques based on conventional lasers can be developed. The direct use of FEL lasers in everyday surgical practice seems, so far, unrealistic due to the large size and specific requirements of these devices, which make it difficult to cheaply and easily implement surgical techniques based on them in the operating room environment.

4.2. Bioimaging and diffraction methods using X-FEL

Coherent X-ray Diffraction Imaging (CXDI) by using X-ray Free Electron Lasers (X-FEL) are underway methods that are among just about to breakthrough bioimaging and the spatial structure determination of macromolecules, including proteins.

In contrast to the Bragg diffraction on crystals, which records a series of narrow peaks, the scattering of a monochromatic X-ray beam on an object that does not show crystal ordering, with an aperiodic arrangement of atoms, leads to the formation of a "granular", irregular distribution of weak intensities. This type of scattering is also classified as diffraction, and the resulting intensity distribution is called the diffraction pattern. This granular pattern of spots is closely related to the spatial arrangement of the scattering atoms in the aperiodic sample. In the case of a coherent beam, the intensity distribution $I(\boldsymbol{Q}, t)$ can be represented as

$$I(\boldsymbol{Q}, t) = A\, S_{\text{coherent}}(\boldsymbol{Q}, t) = A \left| \sum_j f_j(\boldsymbol{Q})\, \mathrm{e}^{\mathrm{i}\boldsymbol{Q}\boldsymbol{R}_j(t)} \right|^2, \tag{9}$$

where f_j is the scattering coefficient of j-th atom, $\boldsymbol{Q}$ is the diffraction vector, $\boldsymbol{R}_j$ is the position vector of j-th atom, and A is a proportionality coefficient. The summation extends to all atoms in the coherence region $V_\mathrm{c} = \xi_t^2 \xi_l$ (where ξ_t and ξ_l denotes transverse and longitudinal coherence, respectively).

The above relationship allows the positions of atoms to be determined if the phases are known [138]. In case of illumination with a beam of insufficient coherence, when the coherence area V_c is smaller than the illuminated sample volume V, the average intensities are recorded as

$$S(\boldsymbol{Q},t) = \left\langle S_{\text{coherent}}(\boldsymbol{Q},t)\right\rangle_{V\gg V_c} \tag{10}$$

which does not allow for the reproduction positions of atoms. Since the intensity of such aperiodic diffraction distribution is very low, a monochromatic beam with a sufficiently large number of coherent photons is necessary for its registration and reconstruction on this basis of the image of the examined object [139–142].

The CXDI method was experimentally demonstrated on 3rd generation synchrotrons for the first time by Miao in 1999 [143], who extended previous experiments on image reconstruction from diffraction in the optical range to the range of X-rays [144]. The first CXDI experiments were performed using the RIKEN undulator station at beamline BL29XUL of the Spring-8 synchrotron. The wavelength used was $\lambda = 0.2$ nm. The tested objects were small *Escherichia coli (E. coli)* bacteria, with a typical size of $0.4\times2\ \mu\text{m}^2$ and a relatively simple internal structure. The bacteria were stained with $KMnO_4$. The reconstructed image had a resolution of about 30 nm, which was 150 times worse as compared to the wavelength of lighting [145].

The obtained resolutions in CXDI experiments on 3rd generation synchrotrons were not particularly high. Due to the parameters of the beams produced by these machines, it would be difficult to significantly improve them. This situation changed radically with the launch, at the beginning of this century, of the first shortwave free electron lasers. Among the most promising new methods using these extremely powerful pulsed X-ray sources are, in particular, CXDI coherent X-ray diffraction imaging.

The radiation damage that develops during a diffraction experiment with the use of classical synchrotron sources fundamentally limits the resolution of diffraction methods. As mentioned before, the protein crystal is able to absorb the maximum dose of about 35 MGy, after which it is practically destroyed. Achieving atomic spatial resolution on the basis of a diffraction image is possible only when the crystal is large enough, which allows to obtain the data statistics necessary to determine the structure with the assumed precision. Thus, using conventional imaging and diffraction methods, atomic resolution cannot be achieved for aperiodic or too small nanocrystalline biological structures. The breakthrough introduced by X-ray free electron lasers results from the breakdown of the barrier associated with this radiation dose limit.

The theory predicts that by illuminating an object with dimensions in the range of 1–1000 nm with ultra-short, intense pulses of coherent X-ray radiation, the diffraction pattern of that object (e.g. a virus particle or a cell) can be recorded before it is destroyed [146]. When the pulse is short enough (< 50 fs), the energy of the photons is absorbed by the object, but the atoms that make it up have no enough time to move significantly from their equilibrium positions before the pulse fades out. Only after the impulse is turned off, the Coulomb explosion develops, leading, in darkness, to the complete disintegration of the object. As a result, the useful radiation doses can increase up to about 600–1000 MGy.

The implementation of this new variant of the CXDI method modified by Neutze [146] is only possible with the previously described SASE–FEL shortwave X-ray source [147]. To achieve atomic resolution, this laser must emit pulses with a wavelength of 0.1 nm and a duration of a dozen fs. The energy of the pulse should be concentrated on the examined object, which means that in the case of diffraction on single protein molecule, it is necessary to focus the beam to size of the order of 100 nm. The actual image of the object is computed from the aperiodic diffraction patterns with aid of phase recovery algorithms. A stream of unbound, free molecules, precisely correlated in time and space with laser pulses is enough to determine the three-dimensional structure of a protein by registering 10^4–10^5 diffraction patterns. Each of them arises as a result of interaction with a new, identical molecule, randomly oriented in space. Therefore, research material in a crystallized form is not required. It is also not necessary to substitute heavy atoms to restore phase information. Both of these features can be crucial in biological research [148, 149].

Among the key properties of X-FEL lasers that condition implementing the idea presented by Neutze is the number of "coherent" photons in a pulse. As it is known, the peak FEL spectral brightness is 109 times greater than that of classic 3rd generation synchrotron sources. Approximately so many times more photons are in the region of coherence in relation to the best 3rd generation synchrotron sources (where the number of coherent photons in this region is of the order of 1).

In recent two decades, the fundamental assumptions of imaging and nanocrystallographic techniques based on CXDI have been experimentally confirmed, using first, among others, XUV-FEL sources FLASH in Hamburg and LCLS at Stanford University, and then transferring the experiments to X-FEL lasers emitting radiation down to a wavelength of 0.1 nm. Already in the first experiments on these devices, a resolution comparable to the wavelength of the source was obtained. An excellent illustration of the CXDI method using X-FEL can be found elsewhere in works on protein diffraction, which describe a recent, groundbreaking experiments concerning the structure of a various protein molecules reconstruction on the basis of diffraction patterns of a large number of individual nanocrystals irradiated consecutively. This method is referred to as serial crystallography. Instead of a stream of single molecules, it records the diffraction from thousands of sequentially illuminated nanocrystals, and then performs a complex analysis consisting in selecting "good" diffraction patterns,

orienting them, and then determining the phase and merging the results. Today, the PDB database contains several hundred structures designated in this way. We are still waiting for single macromolecule imaging with atomic resolution [150].

4.3. Spectroscopic methods using FEL lasers

Although the main research effort using free electron lasers seems to be focused on the development of research related to diffraction imaging and the previously described new methods of crystallography, work has also been underway to apply these unique light sources to study the local electronic structure with spectroscopic methods [151]. In X-ray spectroscopy applications, XFEL lasers are the brightest tunable sources of monochromatic radiation, which gives hope of exploring a number of issues that cannot be resolved with classical sources. The strong femtosecond pulses produced by these new sources are particularly useful for studying the dynamics of even ultrafast biological processes. These include, i.e., processes involving biologically active metallic centers, like some reactions accompanying photosynthesis or the formation and breakdown of molecular bonds [152, 153]. The femtosecond time scale significantly shifts the limits of time resolution in the study of reaction kinetics by as much as three orders of magnitude, as compared to the picosecond resolution achievable with conventional synchrotron beamlines.

In practice, the experiment, which must take into account the inevitable destruction of the sample after each laser shot, becomes somewhat more complicated. This leads to the need to quickly replace the tested material with another, identical one, before continuation with the next laser pulse reaching the material. So far, several techniques of "refreshing" the investigated material have been developed. The simplest of them is to change the place of the next "shot" on the surface of the substrate, where the substance of interest is deposited. When dealing with a liquid or gaseous material, an infusor can be applied "injecting" fresh portions of the material (e.g. proteins in a solution) to the area of interaction with laser pulses. Details of these methods should be found in the experimental descriptions of publications devoted to specific research.

An additional advantage of XFEL spectroscopy is that there is no need to maintain cryogenic conditions during the measurement. Where only the wavelength used allows, samples can be measured in their native form in the gas or water environment. In the work of Alonso-Mori (2012) [151], the XFEL–XES technique was successfully used for the first time to investigate the charge and spin states, as well as the environment, of ligands of Mn (II) complexes and Mn_2 (III–IV) binuclear complexes in room temperature. The obtained $K_{\beta 1,3}$ XES spectra turned out to be consistent with the spectra recorded at low, non-destructive doses of radiation using synchrotron radiation. Interestingly, as Kern

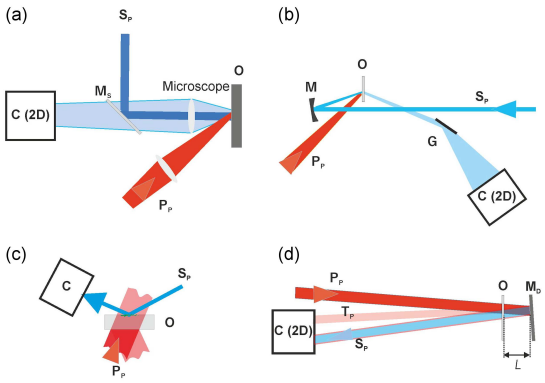

Fig. 8. Diagrams of exemplary measurement systems for pump and probe configurations. (a) The microscopic configuration for surface studies. (b) The spectrographic configuration. (c) The interferometry system. (d) The so-called single-color P&P arrangement. Description: O — sample, MS — semi-transparent mirror/beam splitter, M — concave mirror, MD — delay mirror, C — detector, PP — pumping pulses, SP — sampling pulses, TP — reflection of the pumping pulse recorded on a 2D detector.

and colleagues show [154], XAS measurement with an XFEL source can be used to examine the L-edge of $3d$ transition metals without the need for ultra-high vacuum. It is worth noting that the new design high transmission spectrometer used, equipped with Fresnel zone plates, made it possible to distinguish the Mn_L edge from the strong background of the oxygen edge [155]. By measuring the efficiency of XAS partial fluorescence, information about the oxidation states, symmetry and covalence of the dilute aqueous Mn solution was obtained, suggesting the use of this system for the study of metalloenzymes.

Some researchers believe that sample destruction is a major drawback to methods such as XFEL–XAS in biological applications. Indeed, in some cases more research material may be required, and combining spectroscopic measurement with X-ray imaging or other type of experiments may be complicated. On the other hand, ultra-short femtosecond X-ray pulses from FELs allow us to look into the ultrafast dynamics of processes like speciation of short-lived transient chemical states, e.g. oxidation in redox reactions, which cannot be achieved with other X-ray methods, even with the use of classical synchrotrons.

To study the dynamics of various ultrafast processes with a femtosecond temporal resolution, one of the P&P techniques is commonly used. The material, we intend to study, is pumped to an excited state triggered by a short pulse at the time τ_0, and then at certain time intervals $\Delta\tau_i$ from the pumping pulse we register (we probe) a parameter value, image or spectrum characterizing the state of the process. The triggering pulse does not have to be a light pulse, but we will consider this kind

of pumping system in the following. The triggering and the probing pulses are an appropriately selected short light pulses, of the same or different photon energy, emitted strictly at the moments $\Delta\tau_{\mathrm{i}}$.

Experimental difficulties seem relatively small when we have stable sources, with an intensity low enough not to risk destroying everything that is in the optical path of the beams, especially optics and time intervals $\Delta\tau_{\mathrm{i}}$ do not have to be too short. And, they are in the range at least picoseconds. Figure 8 shows four out of many P&P technique variants used, *inter alia*, with both classical synchrotron sources and free electron lasers.

The use of shortwave FEL lasers to study processes characterized by a time constant in fs–ps range imposes a number of stricter conditions. Usually it is not enough to initiate the process once and then record its course, e.g. in a streak camera, as in the case of classical sources, including synchrotrons. The P&P technique requires the pumping pulses to be synchronized with the sampling pulses, or at least to be able to measure the interval between these pulses with sufficient precision. It is worth realizing that since the speed of light $c = 300$ nm/fs, the wavefront (related, e.g. to the FEL laser pulse) travels a distance of 3 μm within 10 fs. The jitter value achievable for contemporary electronics is, typically, of the order of 10^2 fs. Therefore there is a must to apply more accurate solutions based on optoelectronics exploiting ultrafast physical phenomena. Since with FELs each pulse may destroy the sample, each subsequent measurement must take place after the next "refreshing" of the tested material, so we have the same number of pumping pulses as sampling pulses, only the time between them changes[†15].

Of course, we can reduce the pulse energy of the photon beam by, e.g. the use of attenuators (in the case of FEL, gas attenuators are usually applicable), or de-collimating the beam, but this leads to a reduction in the number of photons interacting with the sample and, consequently, worsens the measured signal. It can also introduce serious modifications to the shape or even destroy the wave fronts, affecting the measurement results (remember that the light emitted by FEL is characterized by a very high coherence, which is crucial for many measurement methods). Let us also pay attention to the difficulties related to the repetition of pulses and the precision of their synchronization. Shortwave FEL lasers use the SASE process (see Sect. 4), which means that the generation and amplification of the radiation pulse occurs spontaneously, starting with a random disturbance at a random location in the undulator. As a result, its energy accumulated while passing through the undulator shows stochastic scatter. The energy value of the individual pulses, and therefore the number of photons they carry is, strictly speaking, unpredictable. In today's SASE–FEL constructions, the width of the energy distribution of these impulses is not great, but for specific values we must refer the reader to the data published for individual machines (one can find them on the Internet as well). There is a method of stabilizing the SASE pulse energy known as seeding, but its adaptation to the FEL case still needs to be refined and disseminated (see, e.g. [156]). So far we have to measure the energy of each impulse and we cannot predict it or plan it precisely. Likewise, the phenomenon of random time deviation between consecutive pulses (sometimes referred to as random time jitter) has more complex causes. Considering very fast processes, we must also take into account random and systematic fluctuations in synchronization between excitation and sampling pulses. When one of the pulse sources is FEL and the other is a synchronized optical laser, which is a typical setup in P&P experiments, the jitter of the time interval between these pulses can severely limit achievable time resolution of a measurement. In order to optimize the impact of this phenomenon and improve the quality of the obtained results, various methods of experiment organization and data analysis are used. One such approach for the Hamburg FLASH laser is presented in [157].

The complexity of the preparation and implementation of a P&P experiment with femtosecond resolution with a source in the form of FEL, and then the analysis of experimental data, is so high that, in order to facilitate the task of less experienced experimenters, sometimes procedures for individual methods and activities are published, along with a model experiment on a specific device. An example is the publication on the study of the ultrafast photochemical process in gas phase molecules using ion imaging performed on the XUV-FLASH in Hamburg [158]. Due to the complexity of the configuration, P&P experiments with free electron lasers require a high level of knowledge and experience as well as very careful preparation and detailed discussions with the scientific teams operating the FEL, optical laser, and measuring station both before and during the experiment. During the experiment itself, it is necessary to precisely determine the spatial and temporal correlation of impulses and to closely monitor all diagnostic and coordinating systems (coupling individual elements). Despite these difficulties, the development of research on ultrafast processes using FEL sources and various spectroscopy methods is growing rapidly, bringing many advances also in the field of biology and medicine.

4.4. Detection and identification of viruses with non-ionizing radiation

Free electron lasers operating in the range of long-wavelength, non-ionizing radiation are among the least commonly used sources of synchrotron

[†15] We pass here over a discussion of an obvious assumption that the process flow is repetitive. If it is not, we may have a serious problem.

radiation today. This looks like a paradox if we consider that the first device of this type, patented by John Madey, was created a quarter of a century before shortwave free electron lasers were constructed [120, 159], which soon took a prominent place among the sources of light necessary for science. Among the reasons for this was probably the fact that the beams produced by these long-wave lasers were competitive primarily in the field of terahertz waves. Yet, until the end of the last century, it was, among others, Due to the lack of sufficiently strong sources of radiation and the shortage of adequately sensitive detectors, the least investigated area, both in terms of the properties of these waves and the possibility of their utilization. This slowed down the development of appropriate measurement technologies and applications even when the free electron lasers of the type created of Madey proved to be an extremely intense and stable THz sources. Only recent years have brought a radical change: the construction of stronger laboratory terahertz sources and since then THz-FELs have quickly become invaluable in many areas of research and practical applications, giving a strong impulse to the development of many areas of experimental terahertz technology.

There is no FEL laser in Poland so far. However, the initiative to build a national source born ten years ago is starting to bear fruit and there is a real chance that in a short time it will be possible to launch the first such machine working in the ultraviolet to terahertz range. In order to familiarize the Reader with the research possibilities of this type of source, we chose one field, which is being intensively developed today due to the outbreak of the COVID-19 viral pandemic. It is the search for highly sensitive methods of pathogen recognition using radiation in the non-ionizing range — terahertz and infrared. Only a small part of the cited works was performed using synchrotron sources, however, it is obvious that THz-FEL sources are great for developing this type of diagnostic technology and then adapting them to the difficult conditions of everyday medical practice.

Rapid detection and characterization of viruses has become particularly important in recent years due to appearance of serious diseases such as Severe Acute Respiratory Syndrome (SARS), Middle Eastern Respiratory Syndrome (MERS), influenza A (H1N1 virus subtype), ZIKA or foodborne diseases [160, 161] and many others. Over the past few decades, a number of virus detection techniques have been developed and disseminated, including the Polymerase Chain Reaction (PCR) and branched-chain DNA Assay (bDNA) [162–164]. The PCR, as well as Reverse Transcription–Polymerase Chain Reaction (RT–PCR) methods are widely used because they enable precise identification through the so-called amplification of target substances, but their detection speed is limited [165]. The PCR, as well as RT–PCR methods are widely used because they enable precise identification through the so-called amplification of target substances, but their detection speed is limited [166]. It has the advantage of being quantifiable, but has a lower detection sensitivity than the PCR method. Bioanalytical techniques are time-consuming and labor-intensive. Therefore, an alternative is sought that enables fast, *in situ* and sensitive detection of pathogens at the nanoscale [167].

The main purpose of the application of terahertz technology is the direct detection of the virus by means of its characteristic absorption signatures revealed in the THz range or the binding of aptamers to the required number of linkers and a suitable substrate to enable direct and selective detection of virus-aptamer complexes. Aptamers are oligonucleotides designed to bind to specific molecules [168, 169]. At the same time, they have a high affinity for the target with which they bind the analyzed molecules, better selectivity and stability than antibodies, are more cost-effective and can be recycled allowing multiple use of the sensor.

It has been shown that terahertz signals with a wavelength of 300 μm provide a good compromise in biological applications between the penetration depth and spatial resolution [170, 171]. Today's plasmonic terahertz structures and microfluidic structures, along with terahertz waveguides, can be easily fabricated using 3 μm photolithography and routine production steps. At photon energies in the range of meV (we have 4.14 meV at 1 THz) terahertz waves can excite some internal degrees of freedom in biological and related molecules. These include, inter alia, H_2O and CO_2 [172, 173], glucose, yeast [174, 175], proteins [176–178], oligonucleotides [179 180], also viruses are examined by terahertz spectroscopy [68, 69, 167]. To concentrate the terahertz electromagnetic signal, most of today's applications use sensors in the form of a butterfly antenna or plasmonic structures. The viral DNA or RNA, if necessary, is detected by the Polymerase Chain Reaction (PCR or RT–PCR, respectively). Other techniques using antibodies and aptamers have also been developed. Together with the fluorescence reading mechanisms they ensure shorter detection times, likewise the analytical PCR method.

The detection and analysis of the absorption spectrum in the THz frequency band related to vibration, torsion and libration modes, as well as to binding states of the biomolecules of interest, is therefore an attractive alternative research method. Its undoubted advantages include the ability to identify molecules without the use of markers [181, 182]. This was demonstrated already in the early 2000s [72, 183–185]. However, relatively long THz wavelengths (300 μm at 1 THz) compared to the size of biomolecules (usually < 100 nm) strongly limited the sensitivity threshold of spectroscopic methods in the THz range (increasing the minimum number of biomolecules necessary for

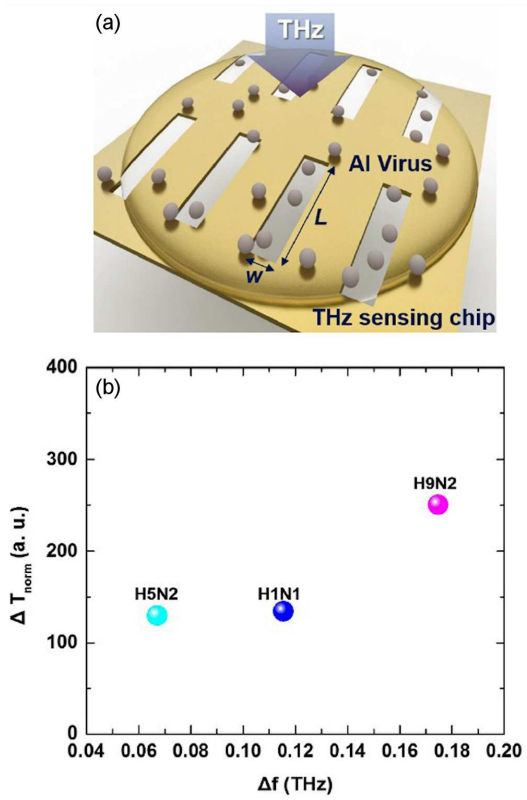

Fig. 9. (a) Conceptual diagram for the virus THz detection in a liquid using a biosensor based on a nano-slotted antenna array. (b) Map showing how the three different virus subtypes tested exhibit characteristic frequency shifts and mass-normalized transmittance changes. Published with permission from [186].

detection). Significant progress has been made by showing that the use of Frequency Selective Surfaces (FSS) with resonant frequencies in the THz range can significantly increase the sensitivity [187]. The FSS is based on a periodic system of resonant metallic structures, "metaatoms", designed to produce sharp resonance in a narrow frequency range [188, 189]. The introduction of a dielectric load in the form of a biomolecule into the FSS changes the resonance frequency compared to an unloaded ("empty") FSS. In THz biosensing, this sensitive mechanism can be used to detect biomolecules even without amplification and using fluorescent markers [187, 190, 191].

Attempts were made to increase the sensitivity of virus detection using a metamaterial composed of terahertz resonators (metaatoms) with a split ring, with different capacitance gap widths [167]. In this way, two types of viruses ranging in size from 60 nm (Pseudomonas virus, PRD1 bacteriophage, DNA) to 30 nm (Escherichia virus, MS2 bacteriophage, RNA) placed on the surface of the metamaterial were detected. The dielectric constants of the viral layers in the THz frequency range were determined previously confirming their high values, convenient for detection. The application of a film of low-density viruses to the surface caused a shift in the resonance frequency of the metamaterial depending on the type of virus. It was higher for the MS2 virus, which has a relatively high dielectric constant. The frequency shift increased with the surface density until saturation, and the sensitivity of the method was determined from the initial slope. Importantly, the sensitivity increased several times when the width of the aperture in metamaterials was reduced from 3 μm to 200 nm. This is due to a combination of geometric factors leading to the enhancement of the electric field accompanying its tight localization.

Three different AI viruses (H5N2, H1N1 and H9N2) were tested in a similar manner using a sensitive THz spectroscopy system assisted by detection chips containing metamaterials (see Fig. 9). The applied system increased the THz field intensity 50 times, leading to a significant improvement in the sensitivity and resolution of the measurement. The different samples of the AI virus could be clearly distinguished in terms of their optical parameters [186].

Measurements by THz Time Domain Spectroscopy (TDS) were also performed to demonstrate the ability to detect bacteriophage viruses PRD1 (60 nm) and MS2 (30 nm). Their sizes range from $\lambda/5000$ to $\lambda/10\,000$ of incident THz waves. Metamaterials were produced with micro- and nanofractures, and changes in metamaterial resonance were observed as a function of virus surface density. The use of THz metamaterials allows to build measuring systems that effectively and repeatably detect even small concentrations of viruses such as PRD1 and MS2. These are, respectively, representatives of double-stranded DNA and single-stranded RNA viruses.

Terahertz reflectance spectroscopy, without plasmonics, was also used to detect the Zika virus using an aptamer designed to bind to capsid proteins [168, 192]. The aptamer formed aptamer-Zika complexes with the virus and was able to capture it on thin-film metallic substrates for more efficient testing using terahertz signals. The constructed terahertz sensor set to detect this virus had a sensitivity of 63 Hz/Zika and gave a minimum detectable signal at $\approx 16 \times 10^3$ viruses. Other substrates such as graphene on Polyethylene Terephthalate (PET), gold foil 50 nm thick on polycarbonate, thin glass (30 mm thick) and teflon were also tested. The graphene substrate was found to allow direct detection of Zika without any aptamers. The authors of this paper suggest that these types of sensors can be easily adapted to detect other viruses such as coronavirus using appropriate aptamers or antibodies.

However, despite the visible advances, the sensitivity of THz detection techniques was until recently still several orders of magnitude lower compared to the sensitivity of the most modern bioanalytical detection techniques. THz techniques still required

significant improvements to achieve the appropriate detection sensitivities needed for real-world applications. Numerous studies with THz techniques have measured biomolecules of comparable Molecular Weight (MW) in aqueous solution. It has been shown that sensitivity increases strongly with MW. As it increases, the minimum detectable concentration decreases because it is easier to detect heavier and larger biomolecules.

DNA composed of four 16-mer sequences with a MW of $\approx$ 19.527 g/mol and a concentration of 4×10^{-6} mol/l can be measured in an aqueous solution by THz spectroscopy and for larger DNA strands of 133 bp (base pairs) with a MW of around 80.942 g/mol, a minimum concentration of 1.23×10^{-9} mol/l was detected by THz spectroscopy in aqueous solution [193, 194]. In contrast, widely accepted bioanalytical tools such as Enzyme Immunoassays (ELISAs) determine Human Serum Albumin (HSA) (MW 66437 g/mol) at concentrations as low as 3.16×10^{-12} mol/l, however by applying a signal amplification [169, 188, 195].

In one study, THz measurements were applied to a liver tumor marker using an FSS-based chip with a microfluidic structure for sample loading [189]. Before the measurement itself, the authors removed the microfluidic channel from the FSS structure and dried the samples with N_2. The antibody and anti-alpha 1 fetoprotein antigen were measured at a MW of $\approx$ 150 000 g/mol and a concentration of 14.6×10^{-9} mol/l. This result represents an increase in sensitivity achieved by FSS-based chips compared to classical terahertz spectroscopic methods. Despite these advances, the detection limits for THz were still about 4 000 times less sensitive than other established bioanalytical techniques.

In the paper by Weisenstein, dated in 2019, but published in 2020 [191], the authors report on the lower detection limit of 1.55×10^{-12} mol/l for MIA cDNA, achieved without PCR amplification, in a modified experimental setup. This is equivalent to 4.64×10^{-18} moles of molecules This is as much as six orders of magnitude better sensitivity than that obtained in other measurements using terahertz radiation, comparable to the results of the best bioanalytical studies. Such a high sensitivity of the measurement was achieved without PCR amplification and without the support of markers. In combination with the very high selectivity (specificity) observed in the same experiment, it paves the way for wider application of THz biosensor techniques in biomedical diagnostics.

TABLE V

Expansion of some common acronyms and abbreviations applied in biomedical research with synchrotron radiation.

Abbreviation	Expansion — meaning
AFM	Atomic Force Microscope
ASNOM	Apertureless SNOM
Bio XAS	Biological X-ray Absorption Spectroscopy
BM	Bending Magnet
bp	Base Pair, i.e., fundamental unit of double-stranded nucleic acids, the building blocks of the DNA double helix
CAI	Conventional Absorption Imaging
CT	Computed Tomography
DAFS	Diffraction Anomalous Fine Structure
EDXA	Energy Dispersive X-ray Analysis
EXAFS	Extended X-ray Absorption Fine Structure
FEL	Free Electron Laser
FELIX	Free-Electron Laser for Infrared Experiments (also the name of the laser in Nijmegen, the Netherlands)
FSS	Frequency Selective Surface
KES	K-edge Subtraction = Dichromography
MALDI	Matrix Assisted Laser Desorption Ionization
MIR	Multiple Image Radiography
MM	Metamaterial
MRT	Microbeam RadioTherapy
NEXAFS	Near-Edge X-ray Absorption Fine Structure
NSOM	$\rightarrow$ SNOM
PAT	Photon Activated Therapy
PCI	Phase Contrast Imaging
PCR	Polymerase Chain Reaction
PIRL	Picosecond-Infrared Laser
P&P	Pump and Probe, Pump-Probe technique
RT–PCR	Reverse Transcription–Polymerase Chain Reaction
SAD	Single Anomalous Diffraction
SASE	Self-Amplified Spontaneous Emission
SAXS	Small Angle X-ray Scattering
SCW	Super Conducting Wiggler
SFX	Serial Femtosecond Crystallography
SNOM	Scanning Near-Field Optical Microscopy
SR	synchrotron radiation
SR-μCT	SR-X-ray Computed Microtomography
TDS	Time-Domain Spectroscopy
u	undulator
USAXS	Ultra-Small Angle X-ray Scattering
w	wiggler
WAXS	Wide Angle X-ray Scattering
XAFS	X-ray Absorption Fine Structure
XANES	X-ray Absorption Near Edge Spectroscopy
μCT	Micro-CT

5. Summary

Due to the size and high operating costs of the synchrotron radiation sources, synchrotrons and free electron lasers are mostly classified as Large Scale Facilities (LSF). In the field of biology and medicine, they are rarely used for routine, mass tasks, such as performing standard tests, patient treatments or industrial production of anything. Compared to other types of sources, their advantages are the unparalleled properties of the emitted beams: high intensity and polarization, high collimation and coherence, together with stability and flexibility, making it possible to adjust to particular needs. The pulsed structure of beam emission simplifies the dynamics studies of biological processes with picosecond (e.g. synchrotrons) and femtosecond (e.g. FELs) temporal resolution. With SR it is also easier to precisely determine the radiation dose than with conventional laboratory sources. For these reasons, synchrotrons and FEL lasers are es-

pecially suitable for tasks such as fundamental research and work aimed at developing a new method, device, precise determination of the conditions necessary to optimize the operation of an instrument or technology.

Biological and medical sciences owe significant progress to synchrotron radiation in areas, such as the determination of the structure of biomolecules, kinetics of biochemical reactions, the development of new and improvement of classical methods of biomedical imaging, the study of the mechanisms of radiation damage and many others. In some areas, such as the study of the protein structure and dynamics, or the development of new methods of photon radiotherapy the impact of SR is leading and will undoubtedly grow in the coming years.

6. Appendix — handy glossary of acronyms and abbreviations

Expansion of some common acronyms and abbreviations applied in biomedical research with synchrotron radiation are listed in Table V.

References

[1] *Advanced High-Resolution Tomography in Regenerative Medicine*, Eds. A. Giuliani, A. Cedola, Springer International Publishing, 2018.

[2] D.C. Creagh, *Radiation in Art and Archeometry*, Elsevier Science, Amsterdam 2000.

[3] G. Artioli, *Scientific Methods and Cultural Heritage: An Introduction to the Application of Materials Science to Archaeometry and Conservation Science*, University Press, Oxford 2010.

[4] I. Bukreeva, G. Ranocchia, V. Formoso, M. Alessandrelli, M. Fratini, L. Massimi, A. Cedola, *Investigation of Herculaneum Papyri by X-Ray Phase-Contrast Tomography*, in: *Nanotechnologies and Nanomaterials for Diagnostic, Conservation and Restoration of Cultural Heritage*, Elsevier, 2019, p. 299.

[5] V. Mocella, E. Brun, C. Ferrero, D. Delattre, *Nat. Commun.* **6**, 1 (2015).

[6] H.-E. Mahnke, T. Arlt, D. Baum, *J. Cult. Herit.* **41**, 264 (2020).

[7] R. Chang, K. Goldsby, *Chemistry*, 12th ed., McGraw-Hill Education, New York 2015, p. 49.

[8] E.P. Solomon, L.R. Eldra-Berg, D.W. Linda-Martin, *Biology*, Brooks/Cole, USA 2010.

[9] D.R. White, J. Booz, R.V. Griffith, J.J. Spokas, I.J. Wilson, *J. ICRU* **os23**, NP (1989).

[10] R. Milo, R. Phillips, *Cell Biology by the Numbers*, Taylor & Francis Ltd., 2016, p. 69.

[11] L.L Barton, F. Goulhen, M. Bruschi, N.A. Woodards, R. Plunkett, F.J. Rietmeijer, *Biometals* **20**, 291 (2007).

[12] L.H. Hartwell, *J. Bacteriol.* **104**, 1280 (1970).

[13] A.K. Bryan, A. Goranov, A. Amon, S.R. Manalis, *PNAS* **107**, 999 (2010).

[14] M. L. Quillin, B.W. Matthews, *Acta Cryst.* **D56**, 791 (2000).

[15] J. Aizenberg, A. Tkachenko, S. Weiner, L. Addadi, G. Hendler, *Nature* **412**, 819 (2001).

[16] W.E. Harris, D.W. Forman, R.D. Battell, M.T.R. Battell, A.K. Nelson, P.F. Brain, *Int. J. Odonatol.* **14**, 281 (2011).

[17] T.E. Sherk, *J. Exp. Zool.* **203**, 61 (1978).

[18] S. Kinoshita, S. Yoshioka, J. Miyazaki, *Rep. Prog. Phys.* **71**, 76401 (2008).

[19] S. Zhu, D. Zhang, Z. Chen, J. Gu, W. Li, H. Jiang, G. Zhou, *Nanotechnology* **20**, 315303 (2009).

[20] H. Arwin, T. Berlind, B. Johs, K. Järrendahl, *Opt. Express* **21**, 22645 (2013).

[21] H. Arwin, A. Mendoza-Galván, R. Magnusson, A. Andersson, J. Landin, K. Järrendahl, E. Garcia-Caurel, R. Ossikovski, *Opt. Lett.* **41**, 3293 (2016).

[22] H. Mouritsen, *The Magnetic Senses*, in: *Neurosciences — From Molecule to Behavior: A University Textbook*, Eds. C.G. Galizia, P.-M. Lledo, Springer, Heidelberg 2013, p. 427.

[23] D. Heyers, D. Elbers, M. Bulte, F. Bairlein, H. Mouritsen, *J. Comp. Physiol. A* **203**, 491 (2017).

[24] R. Wiltschko, W. Wiltschko, *J. R. Soc. Interface* **16**, 20190295 (2019).

[25] E.P. Malkemper, D. Kagerbauer, L. Ushakova, S. Nimpf, P. Pichler, C.D. Treiber, M. de Jonge, J. Shaw, D.A. Keays, *Curr. Biol.* **29**, R14 (2019).

[26] A.J. Cozzone, in: *Encyclopedia of Life Sciences*, 2002, p. 20198.

[27] Portal UniProt or new website of UniProt.

[28] Y. Lu, *Angew. Chem. Int. Ed.* **45**, 5588 (2006).

[29] R.W. Strange, M. Ellis, S.S. Hasnain, *Coord. Chem. Rev.* **249**, 197 (2005).

[30] *Metallomics*, Ed. M.A.Z. Arruda, Springer International Publishing, 2018.

[31] R.H. Holm, P. Kennepohl, E.I. Solomon, *Chem. Rev.* **96**, 2239 (1996).

[32] Y. Gao, C. Chen, Z. Chai, *J. Anal. At. Spectrom.* **22**, 856 (2007).

[33] I. Ascone, R. Strange, *J. Synchrotron Radiat.* **16**, 413 (2009).

[34] M. Jaskolski, *Acta Phys. Pol. A* **117**, 257 (2010).

[35] R. Meuli, Y. Hwu, J. Je, G. Margaritondo, *Eur Radiol.* **14**, 1550 (2004).

[36] For example, the P07 HEMS beamline of the Petra III synchrotron in Hamburg delivers photons in the range of 50 keV–200 keV (down to 0.0062 nm). The ID15A beamline at ESRF in Grenoble, provide in the energy range of 20 keV–500 keV (access May, 2020). In older sources, the range of 30.1–750 keV was even reported for the same beamline.

[37] D. Sayre, H.N. Chapman, *Acta Cryst.* **A51**, 237 (1995).

[38] J.D. Jackson, *Classical Electrodynamics*, Wiley, New York 1975 p. 291.

[39] B.L. Henke, E.M. Gullikson, J.C. Davis, *Atom. Data and Nucl. Tables* **54**, 181 (1993).

[40] G.M. Hale, M.R. Querry, *Appl. Opt.* **12**, 555 (1973).

[41] J.H. Hubbell, S.M. Seltzer, The NIST table (access May, 2020), Tables of X-Ray Mass Attenuation Coefficients and Mass Energy-Absorption Coefficients from 1 keV to 20 MeV for Elements Z = 1 to 92 and 48 Additional Substances of Dosimetric Interest.

[42] K. Beis, G. Evans, *Protein Crystallography: Challenges and Practical Solutions*, Royal Society of Chemistry, Cambridge 2018.

[43] *Protein Crystallography, Methods and Protocols*, Eds. A. Wlodawer, Z. Dauter, M. Jaskólski, Springer, New York 2017.

[44] J. Drenth, J.R. Mesters, *Principles of Protein X-Ray Crystallography*, Springer-Verlag GmbH, 2007.

[45] M.A. Grotzer, E. Schültke, E. Bräuer-Krisch, J.A. Laissue, *Phys. Medica* **31**, 564 (2015).

[46] E. Bräuer-Krisch, J.-F. Adam, E. Alagoz et al., *Phys. Medica* **31**, 568 (2015).

[47] E. Spiller, *Adv. X-ray Analysis* **42**, 297 (2000).

[48] T. Takeda, *Nucl. Instrum. Meth. Phys. Res. A* **548**, 38 (2005).

[49] J.H. Hubbell, *Int. J. Appl. Radiat. Isot.* **33**, 1269 (1982).

[50] Z. Alfassi, *Determination of Trace Elements*, Balaban Publishers VCH, Rehovot 1994.

[51] A. Kabata-Pendias, A.B. Mukherjee, *Trace Elements from Soil to Human*, Springer-Verlag, 2007.

[52] K. Chojnacka, *Recent Advances in Trace Elements*, John Wiley & Sons, Newark (NJ) 2018.

[53] *Int. Symposium on Trace Elements in Man and Animals, 10th Evian-les-Bains, France 1999*, Eds. A.M. Roussel, R.A. Anderson, A.E. Favier, Kluwer Academic, New York 2000.

[54] *Trace Elements and Minerals in Health and Longevity*, Eds. M. Malavolta, E. Mocchegiani, Springer International Publishing, 2018.

[55] B. Markert, *Sci. Total Environ.* **155**, 221 (1994).

[56] B. Markert, S. Fränzle, S. Wünschmann, *Chemical Evolution — The Biological System of the Elements*, Springer International Publishing, 2015.

[57] R. Ortega, G. Devès, A. Carmona, *J. R. Soc. Interface* **6**, S649 (2009).

[58] A. Carmona, G. Devès, R. Ortega, *Anal. Bioanal. Chem.*, **390**, 1585 (2008).

[59] C.J. Fahrni, *Curr. Opin. Chem. Biol.* **11**, 121 (2007).

[60] L.H. Ahrens, *Ionization Potentials: Some Variations, Implications, and Applications*, Pergamon Press, Oxford 1983.

[61] F.A. Cotton, *Science* **298**, 1971 (2002).

[62] A. Vogel, V. Venugopalan, *Chem. Rev.* **103**, 577 (2003).

[63] J. Jagger, *Introduction to Research in Ultraviolet Photobiology*, Prentice-Hall, Engelwood Cliffs (NJ) 1967.

[64] M.E. Bauer, *Proc. IEEE* **73**, 1071 (1985).

[65] *Photon Vegetation Interactions: Applications in Optical Remote Sensing and Plant Ecology*, Eds. R.B. Myneni, I.U. Ross, Springer, 1991.

[66] T.C. Vogelmann, L.O. Björn, *Physiol. Plant.* **60**, 361 (1984).

[67] F.C. De Lucia, *Spectroscopy in the terahertz spectral region*, in: *Sensing with Terahertz Radiation*, Ed. D. Mittleman, Springer, Berlin 2003, p. 39.

[68] M. Brehm, T. Taubner, R. Hillenbrand, F. Keilmann, *Nano Lett.* **6**, 1307 (2006).

[69] A. Zayats, D. Richards, *Nano-Optics and Near-Field Optical Microscopy*, Artech House, Boston 2009.

[70] J.W. Bowen, *Terahertz Sensing at the Nanoscale*, in: *NATO Science for Peace and Security Series B: Physics and Biophysics*, Springer, Netherlands 2017, p. 223.

[71] B.S. Ferguson, H. Liu, S. Hay, D. Findlay, X-C. Zhang, D. Abbott, *Proc. SPIE, Int. Soc. Opt. Eng.* **5275**, 304 (2004).

[72] A.G. Markelz, A. Roitberg, E.J. Heilweil, *Chem. Phys. Lett.* **320**, 42 (2000).

[73] T.R. Globus, D.L. Woolard, T. Khromova, T.W. Crowe, M. Bykhovskaia, B.L. Gelmont, J. Hesler, A.C. Samuels, *J. Biol. Phys.* **29**, 89 (2003).

[74] Z. Yan, Y. Ying, H. Zhang, H. Yu, *Proc. SPIE* **6373**, 63730R-1-10 (2006).

[75] S.E. Peltek, T.N. Goryachkovskaya, V.A. Mordvinov, V.M. Popik, M.A. Scheglov, A.S. Kozlov, S.B. Malyshkin, A.K. Petrov, in: *33rd Int. Conf. on Infrared, Millimeter and Terahertz Waves, Pasadena (CA)*, IEEE, 2008.

[76] G. Kulipanov, N. Gavrilov, B. Knyazev et al., *Terahertz Sci. Technol.* **1**, 107 (2008).

[77] M. Kwiatkowski, M. Wurlitzer, A. Krutilin et al., *J. Proteomics* **134**, 193 (2016).

[78] M. Kwiatkowski, M. Wurlitzer, M. Omidi, L. Ren, S. Kruber, R. Nimer, W.D. Robertson, A. Horst, R.J.D. Miller, H. Schlüter, *Angew. Chem. Int. Ed.***54**, 285 (2014).

[79] Data obtained from information on the BioSync website dedicated to synchrotron lines for the study of biological macromolecules (access May, 2020).

[80] *Radiation Chemistry of Macromolecules*, Ed. M. Dole, Vol. 2, Academic Press, New York 1973.

[81] H. Box, *Radiation Effects: ESR and ENDOR Analysis*, Academic Press, New York 1977.

[82] R. Glaeser, M. Facciotti, P. Walian, S. Rouhani, J. Holton, A. MacDowell, R. Celestre, D. Cambie, H. Padmore, *Biophys. J.* **78**, 3178 (2000).

[83] H. Winick, *J. Synchrotron Radiat.* **5**, 168 (1998).

[84] H. Winick, in: *Proc. of the 1997 Particle Accelerator Conference, Vancouver 1997* (Cat. No.97CH36167) IEEE, 2002, p. 37.

[85] M.E. Couprie, *Nucl. Instrum. Methods Phys. Res. Sect. B* **364**, 4 (2015).

[86] J.M. Holton, K.A. Frankel, *Acta Cryst. D* **66**, 393 (2010).

[87] T. Teng, K. Moffat, *J. Synchrotron Radiat.* **9**, 198 (2002).

[88] J.M. Holton, *J. Synchrotron Radiat.* **16**, 133 (2009).

[89] H. Nikjoo, D.T. Goodhead, *Phys. Med. Biol.* **36**, 229 (1991).

[90] H. Nikjoo, D.E. Charlton, D.T. Goodhead, *Adv. Space Res.* **14**, 161 (1994).

[91] K.M. Prise, M. Folkard, B.D. Michael, B. Vojnovic, B. Brocklehurst, A. Hopkirk, I.H. Munro, *Int. J. Radiat. Biol.* **76**, 881 (2000).

[92] J.F. Ward, *Prog. Nucl. Acid Res. Mol. Biol.* **35**, 95 (1988).

[93] E.F. Garman, S.M. McSweeney, *J. Synchrotron Radiat.* **14**, 1 (2007).

[94] E.F. Garman, M. Weik, *J. Synchrotron Radiat.* **24**, 1 (2017).

[95] E.F. Garman, M. Weik, *J. Synchrotron Radiat.* **26**, 907 (2019).

[96] *An Introduction to Medical Physics*, Ed. M. Maqbool, Springer, 2017.

[97] B. Boudaiffa, P. Cloutier, D. Hunting, M.A. Huels, L. Sanche, *Science* **287**, 1658 (2000).

[98] A. Goytisolo, E. Samper, J. Martın-Caballero, P. Finnon, E. Herrera, J.M. Flores, S.D. Bouffler, M.A. Blasco, *J. Exp. Med.* **192**, 1625 (2000).

[99] G. Heidenthal, *Genetics* **30**, 197 (1945).

[100] D.D. Horikawa, T. Sakashita, C. Katagiri et al., *Int. J. Radiat. Biology* **82**, 843 (2006).

[101] E. Jolivet, S. L'Haridon, E. Corre, P. Forterre, D. Prieur, *Int. J. Syst. Evol. Microbiol.* **53**, 847 (2003).

[102] C. Mothersill, C.B. Seymour, M.C. Joiner, *Radiat. Res.* **157**, 526 (2002).

[103] C. Mothersill, A. Rusin, C. Fernandez-Palomo, C. Seymour, *Int. J. Radiat. Biol.* **94**, 696 (2017).

[104] M. Sokolov, R. Neumann, *Biomed. Rep.* **9**, 99 (2018).

[105] T. Teng, K. Moffat, *J. Synchrot. Radiat.* **7** 313-317 (2000).

[106] P. Sliz, S.C. Harrison, G. Rosenbaum, *Structure* **11**, 13 (2003).

[107] C. Nave, M.A. Hill, *J. Synchrot. Radiat.* **12**, 299 (2005).

[108] J.W. Murray, E.F. Garman, R.B.G. Ravelli, *J. Appl. Cryst.* **37**, 513 (2004).

[109] R.L. Owen, E. Rudino-Pinera, E.F. Garman, *Proc. Natl. Acad. Sci.* **103**, 4912 (2006).

[110] K.S. Paithankar, R.L. Owen, E.F. Garman, *J. Synchrot. Rad.* **16**, 152 (2009).

[111] K.S. Paithankar, E.F. Garman, *Acta Crystallogr. D* **66**, 381 (2010).

[112] G.P. Bourenkov, A.N. Popov, *Acta Crystallogr. D* **66** 409 (2010).

[113] C. Riekel, M. Burghammer, G. Schertler, *Curr. Opin. Struct. Biol.* **15**, 556 (2005).

[114] D. Axford, R.L. Owen, J. Aishima et al., *Acta Crystallogr. D* **68**, 592 (2012).

[115] O.B. Zeldin, M. Gerstel, E.F. Garman, *J. Appl. Cryst.* **46**, 1225 (2013).

[116] O.B. Zeldin, S. Brockhauser, J. Bremridge, J. M. Holton, E. F. Garman, *PNAS* **110**, 20551 (2013).

[117] RADDOSE-3D (access May, 2021).

[118] J.B. Pełka, K.R. Tybor, R. Nietubyc, G. Wrochna, *Acta Phys. Pol. A* **117**, 427 (2010).

[119] J. Ovelmen-Levitt, K.D. Straub, S. Hauger, E. Szarmes, J. Madey, R.D. Pearlstein, B.S. Nashold, *Lasers Surg. Med.* **33**, 81 (2003).

[120] J.M.J. Madey, *J. Appl. Phys.* **42**, 1906 (1971).

[121] L.R. Elias, W.M. Fairbank, J.M.J. Madey, H.A. Schwettman, T.I. Smith, *Phys. Rev. Lett.* **36**, 717 (1976).

[122] D.A.G. Deacon, L.R. Elias, J.M.J. Madey, G.J. Ramian, H.A. Schwettman, T.I. Smith, *Phys. Rev. Lett.* **38**, 892 (1977).

[123] S. Khan, *J. Mod. Opt.* **55**, 3469 (2008).

[124] V.N. Litvinenko, S.H. Park, I.V. Pinayev, Y. Wu, *Nucl. Instrum. Methods Phys. Res. A* **475**, 195 (2001).

[125] K. Tiedtke, A. Azima, N. von Bargen et al., *New J. Phys.* **11**, 1 (2009).

[126] N. Patel, *Nature* **415**, 110 (2002).

[127] G. Wrochna, J. Jagielski, J. Krzywinski, R. Nietubyc, J. Pełka, E. Pławski, J. Sekutowicz, R. Sobierajski, J. Szewiński, *Synchrotron Rad. Nat. Sci.* **8**, 3 (2009)

[128] B. Jean, *Nucl. Instrum. Methods Phys. Res. A* **393**, 540 (1997).

[129] G.S. Edwards, R.H. Austin, F.E. Carroll et al., *Rev. Sci. Instrum.* **74**, 3207 (2003).

[130] G.S. Edwards, M.S. Hutson, *J. Synchrotron Radiat.* **10**, 354 (2003).

[131] W. Wagner, A. Sokolow, R. Pearlstein, G. Edwards, *Appl. Phys. Lett.* **94**, 013901 (2009).

[132] J.I. Youn, P. Sweet, G.M. Peavy, *Lasers Surg. Med.* **39**, 332 (2007).

[133] M. Heya, S. Sano, N. Takagi, Y. Fukami, K. Awazu, *Lasers Surg. Med.* **32**, 349 (2003).

[134] M.L. Copeland, R.J. Maciunas, G.S. Edwards, in: *Neurosurgical Topics: Advanced Techniques in Central Nervous System Metastases* Ch. VII, Ed. R.J. Maciunas, The American Association of Neurological Surgeons, Park Ridge (IL) 1998.

[135] K.M. Joos, J.H. Shen, D.J. Shetlar, V.A. Casagrande, *Lasers Surg. Med.* **27**, 191 (2000).

[136] G.S. Edwards, *Laser Photonics Rev.*, **3**, 545 (2009).

[137] V.N. Litvinenko, S.H. Park, I.V. Pinayev, Y. Wu, M. Emamian, N. Hower, P. Morcombe, O. Oakeley, G. Swift, P. Wang, *Nucl. Instrum. Methods Phys. Res. A* **429**, 151 (1999).

[138] D.L. Abernathy, G. Grübel, S. Brauer, I. McNulty, G.B. Stephenson, S.G.J. Mochrie, A.R. Sandy, N. Mulders M. Sutton, *J. Synchrotron Rad.* **5**, 37 (1998).

[139] S.K. Sinha, M. Tolan, A. Gibaud, *Phys. Rev. B* **57**, 2740 (1998).

[140] G. Grübel, F. Zontone, *J. Alloys Compd.* **362**, 3 (2004).

[141] J.W. Goodman, *Statistical Properties of Laser Speckle Patterns*, in: *Laser Speckle and Related Phenomena*, Ed. J.C. Dainty, Springer, Berlin 1975, p. 9.

[142] G. Parry, *Speckle Patterns in Partially Coherent Light*, in: *Laser Speckle and Related Phenomena*, Ed. J.C. Dainty, Springer, Berlin 1975, p. 77.

[143] J. Miao, P. Charalambous, J. Kirz, D. Sayre, *Nature* **400**, 342 (1999).

[144] J.R. Fienup, *J. Opt. Soc. Am. A* **4**, 118 (1987).

[145] J. Miao, K.O. Hodgson, T. Ishikawa, C.A. Larabell, M.A. LeGros, Y. Nishino, *Proc. Natl. Acad. Sci.* **100**, 110 (2003).

[146] R. Neutze, R. Wouts, D, van der Spoel, E. Weckert, J. Hajdu, *Nature* **406**, 752 (2000).

[147] R. Bonifacio, C. Pellegrini, L.M. Narducci, *Opt. Commun.* **50**, 373 (1984).

[148] R. Neutze, G. Huldt, J. Hajdu, D. van der Spoel, *Radiat. Phys. Chem.* **71**, 905 (2004).

[149] H.N. Chapman, A. Barty, M.J. Bogan et al., *Nat. Phys.* **2**, 839 (2006).

[150] A. Aquila, A. Barty, *Single Molecule Imaging Using X-ray Free Electron Lasers*, in: *X-ray Free Electron Lasers*, Springer International Publishing, 2018, p. 401.

[151] R. Alonso-Mori, J. Kern, R.J. Gildea et al., *Proc. Natl. Acad. Sci.* **109**, 19103 (2012).

[152] T. Ishikawa, H. Aoyagi, T. Asaka et al., *Nat. Photonics* **6**, 540 (2012).

[153] F. Porcaro, S. Roudeau, A. Carmona, R. Ortega, *Trend. Anal. Chem.* **104**, 22 (2018).

[154] J. Kern, V.K. Yachandra, J. Yano, *Curr. Opin. Struct. Biol.* **34**, 87 (2015).

[155] R. Mitzner, J. Rehanek, J. Kern et al., *J. Phys. Chem. Lett.* **4**, 3641 (2013).

[156] E. Allaria, F. Bencivenga, R. Borghes et al., *Nat. Commun.* **4**, 1 (2013).

[157] E. Savelyev, R. Boll, C. Bomme et al., *New J. Phys.* **19**, 43009 (2017).

[158] D. Rolles, R. Boll, B. Erk, D. Rompotis, B. Manschwetus, J. Visualized Exp. **140**, (2018).

[159] *X-Ray Free Electron Lasers*, Eds. U. Bergmann, V.K. Yachandra, J. Yano, Royal Society of Chemistry, 2017.

[160] P.S. Mead, L. Slutsker, V. Dietz, L.F. McCaig, J.S. Bresee, C. Shapiro, P.M. Griffin, R.V. Tauxe, *States Emerg. Infect. Dis.* **5**, 607 (1999).

[161] F. Fung, H.-S. Wang, S. Menon, *Biomed. J.* **41**, 88 (2018).

[162] *PCR Technology — Principles and Applications for DNA Amplification*, Ed. H.A. Erlich, Palgrave Macmillan, London 1989.

[163] J. Vinje, *J. Clin. Microbiol.* **53**, 373 (2015).

[164] *RT–PCR Protocols*, Ed. N. King, Humana Press, 2010.

[165] P. Belgrader, *Science* **284**, 449 (1999).

[166] C. Pachl, J.A. Todd, D.G. Kern et al., *J. Acquir. Immune Defic. Syndr. Hum. Retrovirol.* **8**, 446 (1995).

[167] S.J. Park, S.H. Cha, G.A. Shin, Y.H. Ahn, *Biomed. Opt. Express* **8**, 3551 (2017).

[168] S. Dolai, M. Tabib-Azar, "Terahertz Detection of Zika Viruses", *Preprints*, 2020.

[169] A. Ahmadivand, B. Gerislioglu, Z. Ramezani, A. Kaushik, P. Manickam, S.A. Ghoreishi, *Biosens. Bioelectron.* **177**, 112971 (2021).

[170] D. Cheng, X. He, X. Huang, B. Zhang, G. Liu, G. Shu, C. Fang, J. Wang, Y. Luo, *Int. J. RF Microw. Comput.-Aided Eng.* **28**, e21448 (2018).

[171] X. Yang, K. Yang, Y. Luo, W. Fu, *Appl. Microbiol. Biotechnol.* **100**, 5289 (2016).

[172] M. Grechko, T. Hasegawa, F. D'Angelo, H. Ito, D. Turchinovich, Y. Nagata, M. Bonn, *Nat. Commun.* **9**, 1 (2018).

[173] H. Hoshina, Y. Iwasaki, E. Katahira, M. Okamoto, C. Otani, *Polymer* **148**, 49 (2018).

[174] O. Fawole, K. Sinha, M. Tabib-Azar, in: *2015 IEEE SENSORS*, 2015.

[175] O. Fawole, M. Tabib-Azar, in: *2016 IEEE MTT-S International Microwave Symposium (IMS), San Francisco (CA)*, 2016.

[176] S.J. Kim, B. Born, M. Havenith, M. Gruebele, *Angew. Chem. Int. Ed.* **47**, 6486 (2008).

[177] H. Yoshida, Y. Ogawa, Y. Kawai, S. Hayashi, A. Hayashi, C. Otani, E. Kato, F. Miyamaru, K. Kawase, *Appl. Phys. Lett.* **91**, 253901 (2007).

[178] S. Ebbinghaus, S.J. Kim, M. Heyden, X. Yu, M. Gruebele, D.M. Leitner, M. Havenith, *J. Am. Chem. Soc.* **130**, 2374 (2008).

[179] M. Tang, Q. Huang, D. Wei, G. Zhao, T. Chang, K. Kou, M. Wang, C. Du, W. Fu, H.-L. Cui, *J. Biomed. Opt.* **20**, 95009 (2015).

[180] N.T. Bagraev, A.L. Chernev, L.E. Klyachkin, A.M. Malyarenko, A.K. Emel'yanov, M.V. Dubina, *Semiconductors* **50**, 1208 (2016).

[181] H. Fröhlich, *J. Quantum Chem.* **2**, 641 (1968).

[182] W. Zhuang, Y. Feng, E.W. Prohofsky, *Phys. Rev. A* **41**, 7033 (1990).

[183] M. Brucherseifer, M. Nagel, P.H. Bolivar, H. Kurz, A. Bosserhoff, R.Büttner, *Appl. Phys. Lett.* **77**, 4049 (2000).

[184] S.P. Mickan, A. Menikh, H. Liu, C.A. Mannella, R. MacColl, D. Abbott, J. Munch, X.-C. Zhang, *Phys. Med. Biol.* **47**, 3789 (2002).

[185] B.M. Fischer, M. Walther, P.U. Jepsen, *Phys. Med. Biol.* **47**, 3807 (2002).

[186] D.-K. Lee, J.-H. Kang, J. Kwon, J.-S. Lee, S. Lee, D. H. Woo, J. H. Kim, C.-S. Song, Q.-H. Park, M. Seo, *Sci. Rep.* **7**, 1 (2017).

[187] C. Debus, P.H. Bolivar, *Appl. Phys. Lett.* **91**, 184102 (2007).

[188] M.M. Hassan, F.S. Sium, F. Islam, S.M. Choudhury, *Sens. Bio-Sens. Res.* **33**, 100429 (2021).

[189] Z. Geng, X. Zhang, Z. Fan, X. Lv, H. Chen, *Sci. Rep.* **7**, 1 (2017).

[190] C. Debus, G. Spickermann, M. Nagel, P.H. Bolivar, *Microw. Opt. Techn. Let.* **53**, 2899 (2011).

[191] C. Weisenstein, D. Schaar, A.K. Wigger, H. Schäfer-Eberwein, A.K. Bosserhoff, P.H. Bolivar, *Biomed. Opt. Express* **11**, 448 (2019).

[192] K.H. Lee, H. Zeng, *Anal. Chem.* **89**, 12743 (2017).

[193] A. Arora, T.Q. Luong, M. Krüger, Y.J. Kim, C.-H. Nam, A. Manz, M. Havenith, *The Analyst* **137**, 575 (2012).

[194] S. Laurette, A. Treizebre, A. Elagli, B. Hatirnaz, R. Froidevaux, F. Affouard, L. Duponchel, B. Bocquet, *RSC Adv.* **2**, 10064 (2012).

[195] N. Meinzer, W. Barnes, I. Hooper, *Nat. Photonics* **8**, 889 (2014).